nature geoscience

LETTERS

PUBLISHED ONLINE: 15 JANUARY 2012 | DOI: 10.1038/NGEO1373

Stick–slip advance of the Kohat Plateau in Pakistan

S. P. Satyabala[1], Zhaohui Yang[2] and Roger Bilham[2]*

Throughout most of the Himalaya, slip of the Indian Plate is restrained by friction on the interface between the plate and the overlying wedge of Himalayan rocks. Every few hundred years, this interface—or décollement—ruptures in one or more $M_w \geq 8$ earthquakes. In contrast, in the westernmost Himalaya, the Indian Plate slips aseismically beneath wide plateaux fronting the Kohistan Mountains. The plateaux are underlain by viscous décollements that are unable to sustain large earthquakes[1]. Potwar, the widest of these plateaux is underlain by viscous salt[2,3], which currently permits it to slide at rates of about 3 mm yr^{-1} (refs 4,5), much slower than its 2 Myr average[6,7]. This deceleration has been attributed to recently increased friction through the loss of salt from its décollement. Here we use interferometric synthetic aperture radar and seismic data to assess movement of the Kohat Plateau—the narrowest and thickest plateau[8,9]. We find that in 1992 an 80 km^2 patch of the décollement ruptured in a rare M_w6.0 earthquake, suggesting that parts of the décollement are locally grounded. We conclude that this hybrid seismic and aseismic behaviour represents an evolution of the mode of slip of the plateaux from steady creep towards increasingly widespread seismic rupture.

A well-known paradox concerns the impossibility of pushing a wide, heavy slab of rock over a horizontal thrust fault[10,11]. The basal friction resulting from the weight of the slab will rupture the slab elsewhere, rather than permit it to slide on its basal thrust fault. In the face of abundant geological evidence for slip of deep thrust faults, Oldham[10] speculated that perhaps the weight of the rock could be transiently relieved, or that perhaps only a part of the thrust fault would move at any one time, thereby loading contiguous parts of the thrust fault 'akin to the crawl of a caterpillar which advances one part of its body at a time, and all parts in succession'.

We now accept that thrust faults do indeed slip with a caterpillar-like motion—albeit at rupture velocities exceeding 3 km s^{-1}. They do so dynamically. At any one moment less than 10 km of the rocks adjoining the fault are in relative motion, and the rest of the fault locked[12–14]. We also know that in the presence of viscous salt it is possible to reduce the static friction to permit several-km-thick blocks of rock to slide aseismically on a décollement, as has clearly occurred in the Potwar Plateau of Pakistan, the Jura Fold Belt in Europe and the Zagros in Iran. The mobile rock sheets above these salt décollements are characterized by great widths (150–200 km) and narrow wedge angles (≈1°) when compared with thrust faults that occur in subduction zones[11,15–17]. Seismic activity on these décollements and within their overlying sedimentary carapace is rare[18–20].

On 20 May 1992 an unusual $M_w = 6.0$ earthquake occurred beneath the Kohat Plateau (Fig. 1) approximately 30 km north of the Surghar range that bounds its southern edge. The earthquake was larger than any in the historical record[1,19] and caused damage to nearby cities and loss of life in Kohat. The earthquake resulted in surface deformation distinctly visible on interferometric synthetic aperture radar (InSAR) data in tracks 5 and 277 (Fig. 2 and Supplementary Fig. S5). We examined several possible subsurface dislocation geometries before concluding that a subhorizontal rupture at 8 km depth was responsible for the earthquake (Supplementary Information). The best-fitting elastic model accounts for 90% of the surface deformation field and has the following parameters and 1σ uncertainties: depth $7.8^{+2.1}_{-1.5}$ km, dip $1^{+3.2}_{-1.0}$ degrees north, strike N 244^{+5}_{-7} E, width $8^{+3.6}_{-4.1}$ km, length $9.9^{4.5}_{-5.6}$ km, slip 33^{+57}_{-13} cm. When allowance is made for a trade-off in parameters in solution space, and if we use an elastic modulus of 3.5×10^{10} N m^{-2}, the resulting magnitude range is $5.9 < M_w < 6.0$. The depth and dip of the

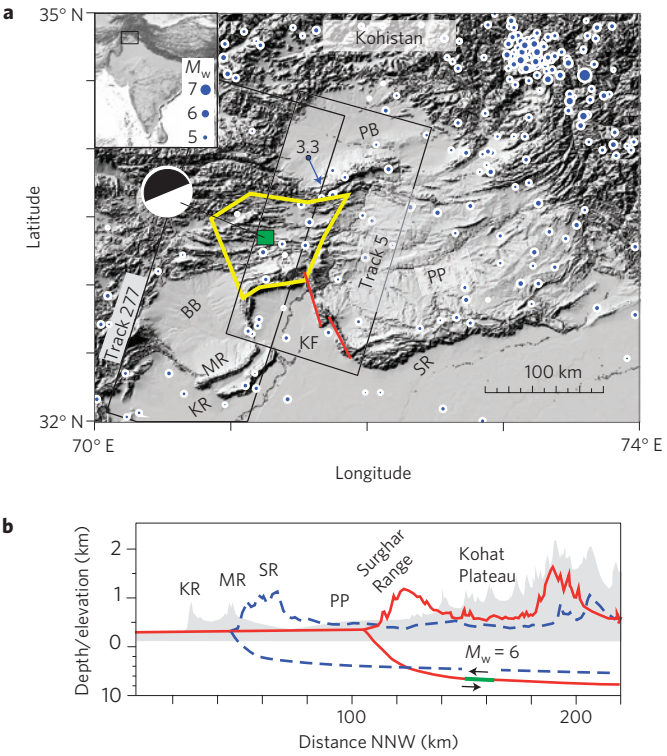

Figure 1 | Kohat Plateau (yellow polygon) flanked by neighbouring plateaux. Rupture area of 20 May 1992 $M_w = 6.0$ earthquake shown as green rectangle in map (**a**) and green line in section (**b**) with inset mechanism. **a**, InSAR tracks numbered as inclined rectangles. The blue arrow indicates the velocity (mm yr^{-1}) of convergence of the Peshawar Basin with the fixed Indian Plate[3]. Seismicity from US Geological Survey Preliminary Determination of Epicenters catalogue 1973–2008 (blue circles with scale top left). **b**, Three sections illustrate the morphology of the Bannu Basin (BB, grey), Potwar Plateau (PP, dashed blue) and Kohat Plateau (red) respectively. KR, Kishor Range; MR, Marwat Range; SR, Salt Range; KF, Kalabagh Fault; PB, Peshawar Basin.

[1]National Geophysical Research Institute, Hyderabad 500031, India, [2]CIRES and Department of Geological Sciences, University of Colorado, Boulder, Colorado 80309-0399, USA. *e-mail: bilham@colorado.edu.

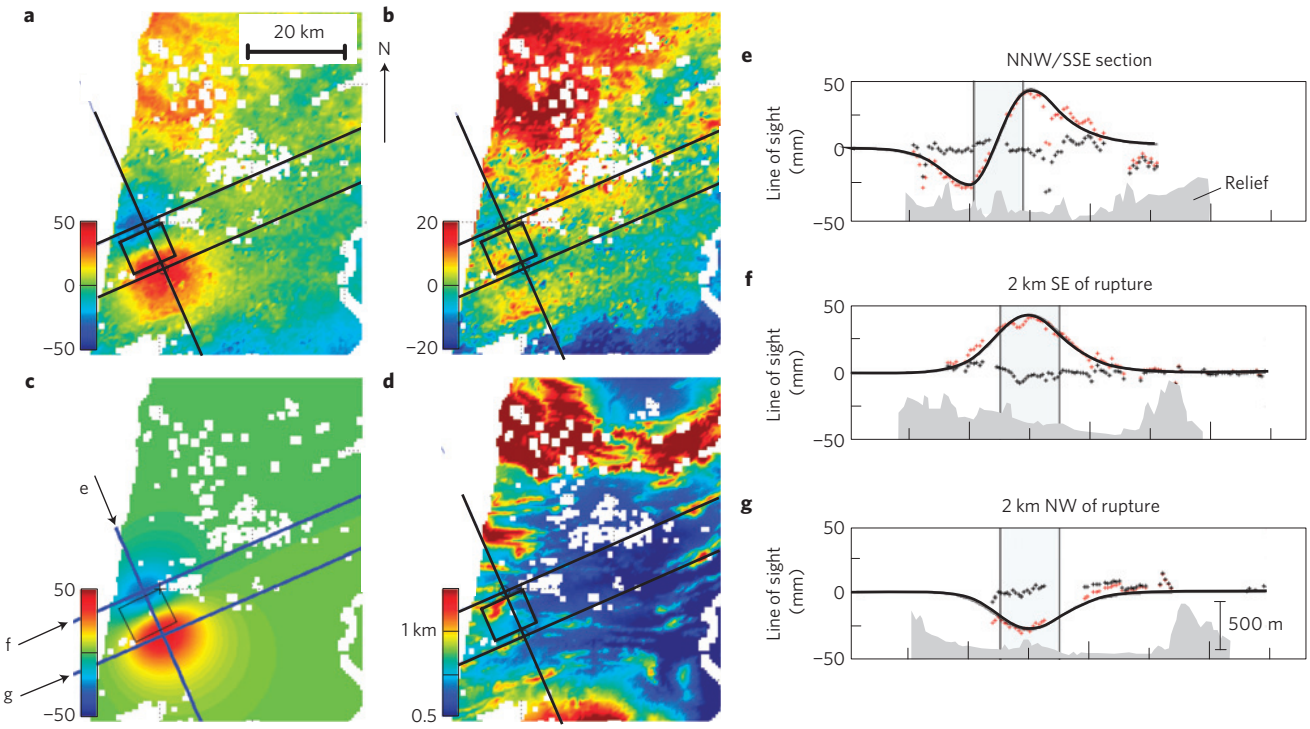

Figure 2 | InSAR interferograms and synthetic model for 1992 earthquake. a, Coseismic interferogram for 157 days after the Kohat earthquake (Supplementary Table S3). **b**, Residual after subtracting synthetic model from **a**. **c**, Synthetic interferogram of best-fitting model (Supplementary Table S2). Line-of-sight displacement scales in mm (**a**–**c**). **d**, Topography for the region. **e**–**g**, Profiles identified in **c**. Continuous line, model; red and black symbols, coseismic and residual data, respectively.

earthquake indicate that seismic rupture occurred on the $2 \pm 1°$ NNW dipping basal décollement underlying the Kohat Plateau, which is inferred from geological and seismic reflection data[18,20,21] to lie at ≈8 km depth.

In contrast to the depth determined from InSAR data, the earthquake was reported teleseismically with a <5° NE dipping thrust mechanism at 16 km depth (Supplementary Table S1). Hypocentral determinations using several depth phases initially placed the earthquake and two aftershocks at 19–27 km (ref. 22), although the mainshock was subsequently assigned a depth of 16 km (ref. 23). Suspecting that the hypocentral depth of the earthquake may have included a substantial depth error caused by low seismic velocities in the plateau[9,18,21], we examined the waveform data from 26 broadband seismic stations that recorded the earthquake worldwide (Supplementary Fig. S2). We used the differences in arrival times of two direct body waves (P, S) and three reflected phases (pP, sP and sS) to estimate the average velocities between the earthquake source and surface in the plateau sediments ($V_p \sim 4\,km\,s^{-1}$, $V_s \sim 2\,km\,s^{-1}$) (Supplementary Information). Our revised focal mechanism (Supplementary Table S1) is consistent with the above InSAR model and teleseismic solutions but differs from one that includes local stations[24]. The magnitude and focal depth obtained from our teleseismic calculations are $M_w = 5.9$ and 8 ± 1 km respectively. The pulse width of ≈2.3 s that best fits the seismic data is consistent with the rupture dimension of 8–10 km calculated from InSAR, and a rupture propagation velocity of $\approx 3.5\,km\,s^{-1}$. Notably, the shear modulus derived from the geometric moment of the earthquake when compared to the teleseismic moment is typical of fault zones elsewhere.

The seismic and InSAR data thus provide compelling evidence that the décollement slipped seismically in 1992. The significance of this is that, for horizontal rupture to have occurred, the patch that was stuck must have been loaded by preseismic stresses developed 30 km north of the frontal thrusts of the Surghar range, and a yet greater distance south of the Kohistan Ranges north of the Peshawar Basin, where currently ≈80% of India's convergence with the EuroAsian plate is manifest geodetically[25]. Thus the asperity is not located at a transition zone between locked seismic rupture and steady creep, as, for example, occurs in subduction zones or near the base of the high Himalaya. The process we observe is similar to that associated with repeating earthquakes on asperities on creeping faults in central California and elsewhere[26–29]. Creep processes apparently permit the plateau to stream around basal asperities, with strain developing upstream and along their sides[27].

We dismiss the possibility that elastic loading of an isolated patch near the centre of the décollement resulted from seismic loading from the north in historical earthquakes. Slip in the 1992 earthquake would take 100 years to be renewed at the present-day observed convergence rate, and the patch that slipped 30 cm in 1992 represents less than 5% of the total area of the Kohat décollement. Thus for the entire plateau to have advanced, domino-like, in a series of contiguous earthquakes, 20 or more events would be required per century for the entire area to slip at least once to keep up with the convergence rate. This would require a $M_w \approx 6$ earthquake once per decade, more than an order of magnitude higher than observed[1,16]. We have searched unsuccessfully for similar deformation fields in the InSAR imagery that may have occurred as slow earthquakes eluding detection by the worldwide seismic array. None are apparent in the period 1992–1997.

Thus cumulative slip of the plateau occurs partly by aseismic slip on a viscous décollement, and partly by seismic slip on one or more asperities where the sediments of the plateau lie directly on the crystalline or sedimentary basement. The décollement beneath the Potwar Plateau is known to consist of EoCambrian salt[1,2]. The petrology of the décollement beneath Kohat Plateau is unknown because it has not been penetrated by drilling, nor is it sensed as a clear reflecting horizon[8,9,20,21], yet a weak layer of compliant

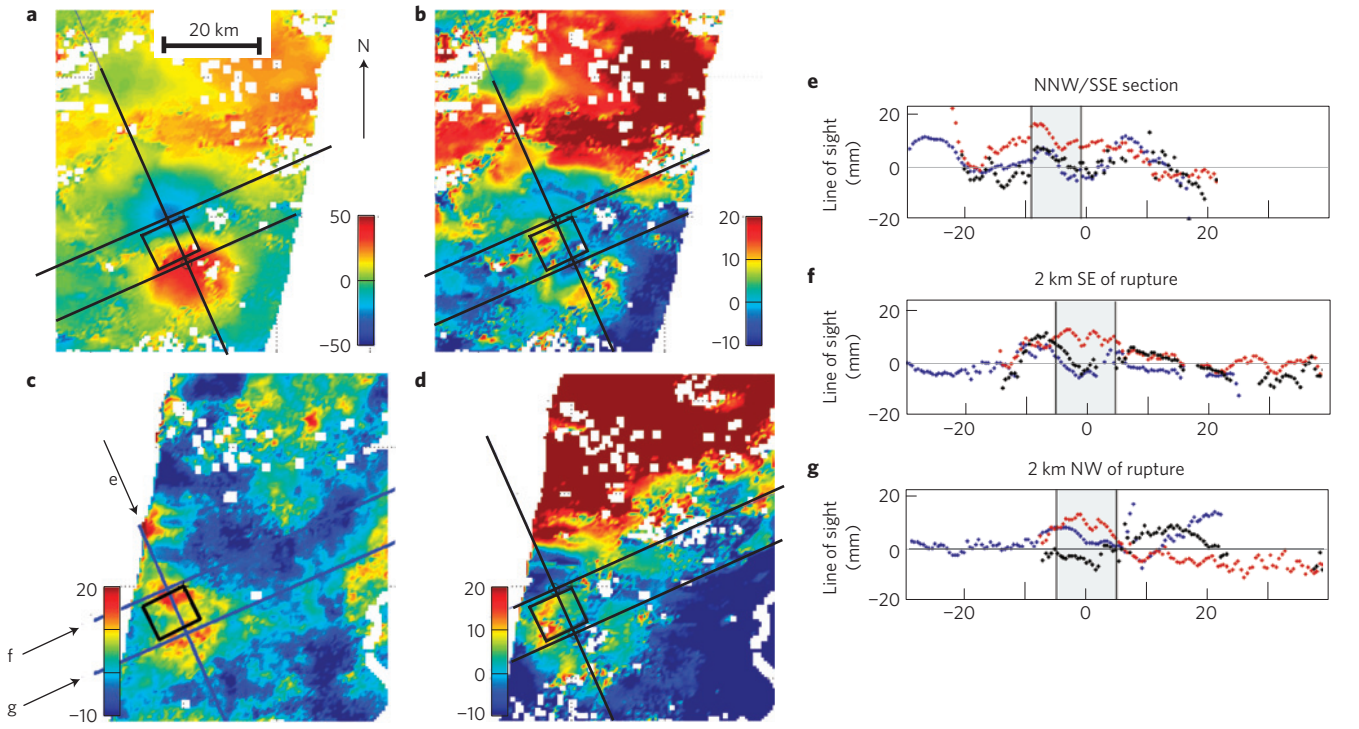

Figure 3 | Post-seismic slip on the décollement (scales in mm). a,**b**, Map views from Track 277 include 2,895 d of afterslip. Synthetic coseismic slip has been removed from **b**. **c**, Afterslip 17–402 d after the earthquake from time-series analysis of a post-seismic 30-fold stack spanning 1992–93 (Supplementary Information). **d**, Map view from Track 5 includes 2,316 d of afterslip with synthetic coseismic slip removed. **e**–**g**, Profiles of residuals identified in **c** as **e**, **f**, **g** respectively. Blue dots from **b**, red from **c** and black from **d**. The grey shaded region in these profiles indicates the location of coseismic rupture.

rheology must exist throughout much of the décollement for aseismic slip to have stressed the 1992 rupture zone. Presumably, the plateau at the location of the 1992 earthquake has been welded to the underlying basement by increased local friction, or has occurred, as in the Potwar Plateau, by the evacuation of viscous materials to the surrounding décollement or into the cores of anticlines developing in association with ramp thrusts[9].

Consistent with the notion that the rupture zone is surrounded by a region where décollement slip is dominantly aseismic, postseismic interferograms reveal slip of 17 ± 9 mm on the décollement in an annulus surrounding the rupture zone (Fig. 3 and Supplementary Fig. S12b). Our analysis indicates that this triggered afterslip was largely complete within 6 months of the earthquake. Although atmospheric noise prevents this afterslip from being quantified spatially, 10 mm of average slip in an annular region ≈5 km wide corresponds to a net additional moment release equivalent to an $M_w = 5.2$ earthquake. Aftershocks were recorded 11, 16 and 20 d after the mainshock within this region of accelerated slip to the east ($m_b = 4.6$), southwest ($m_b = 4.9$) and south ($m_b = 4.4$) respectively of the rupture area (Supplementary Information).

If creep at rates as high as 3.3 mm yr^{-1} were to occur beneath the southern Kohat Plateau, we would anticipate surface deformation to be manifest in the Surghar ranges or between these ranges and the Punjab sediments to their south. We have searched unsuccessfully for this deformation in InSAR imagery. Its absence may be not only because its rate is low, but also because the slip may have occurred parallel to the along-track direction of the InSAR scenes, or because the southward retardation in slip rates is widely distributed and therefore below current noise levels.

A remaining consideration is whether $M_w > 6$ earthquakes could occur on the décollement. If we assume that stress propagates from the north southward facilitated by basal creep, the recent occurrence of the 1992 earthquake leads us to suppose that the most likely location for a future earthquake lies between the southern edge of this rupture and the frontal thrusts of the Surghar Range, a 30×40 km^2 area. If we suppose that slip of 1–2 m ruptured this whole area, the resulting earthquake would be equivalent to an $M_w = 7.0$. Although there is no precedent in the historical record[1], the record is sparse before 1800, and with a loading rate of ≈3 mm yr^{-1} such earthquakes could occur no more frequently than once every 300–600 years. We note that the 1992 earthquake had dimensions comparable to the thickness of the plateau, and comparable to the spacing between prominent mapped anticlines and shear zones of the Kohat Plateau (refs 9,21 and Supplementary Fig. S9). It is thus possible that the structural segmentation of the plateau determines the dimensions of basal ruptures, hence 1992-type earthquakes may represent the maximum-size décollement earthquake that can occur.

The southern Kohat Plateau advances over India partly as a result of creep on a viscous décollement, and partly by stick–slip processes on one or more asperities that for prolonged periods are welded to the underlying basement. Thus this part of the plateau does indeed slip with a caterpillar-like motion as envisaged by Oldham[10]; however, it requires interseismic creep on the décollement, which cannot occur in the presence of significant friction. The geodetic rate of translation of the southern Kohat Plateau has yet to be measured directly but is surely less than the 3 mm yr^{-1} measured with GPS methods on the southern Potwar Plateau[6]. That creep can occur at rates of a few mm yr^{-1} on a shallow foreland thrust fault such as exists throughout the Himalaya is an important observation, because it potentially reduces the slip available for subsequent great earthquakes; however, because the 1992 earthquake is apparently unique, its occurrence is almost certainly attributable to the special rheology of the décollement beneath the plateaux of Pakistan.

Received 26 January 2011; accepted 15 December 2011; published online 15 January 2012

References

1. Martin, S. & Szeliga, W. A catalog of felt intensity data for 589 earthquakes in India: 1636–2009. *Bull. Seismol. Soc. Am.* **100,** 536–569 (2010).
2. Yeats, R. S., Khan, S. H. & Akthar, M. Late quaternary deformation of the Salt Range of Pakistan. *Geol. Soc. Am. Bull.* **95,** 958–966 (1984).
3. Butler, R. W. H., Coward, M. P., Harwood, G. M. & Knipe, R. in *Dynamical Geology of Salt and Related Structures* (eds O'Brien, J. J. & Lerche, I.) 399–418 (Academic, 1987).
4. McDougall, J. W. & Khan, S. H. Strike-slip faulting in a foreland fold–thrust belt: The Kalabagh fault and western Salt Range, Pakistan. *Tectonics* **9,** 1061–1075 (1990).
5. Baker, D. M. *et al*. Development of the Himalayan frontal thrust zone: Salt Range, Pakistan. *Geology* **16,** 3–7 (1988).
6. Khan, M. A. *et al*. Preliminary geodetic constraints on plate boundary deformation on the western edge of the Indian plate from TriGGnet (Tri-University GPS Geodesy Network). *J. Himal. Earth Sci.* **41,** 71–87 (2008).
7. Chen, L. & Khan, S. D. InSAR observation of the strike-slip faults in the northwest Himalayan frontal thrust system. *Geosphere* **6,** 731–736 (2010).
8. Pivnik, D. A. & Sercombe, W. J. in *Compression and Transpression Related Deformation in the Kohat Plateau, NW Pakistan* Vol. 44 (eds Searle, M. P. & Treloar, P.) 559–580 (Himalayan tectonics: Geol. Soc. London Spec. Publ., 1993).
9. Sercombe, W. J. *et al*. Wrench Faulting in the northern Pakistan foreland. *AAPG Bull.* **82,** 2003–2030 (1998).
10. Oldham, R. D. Know your faults. *J. Geol. Soc. Lond.* **77,** 77–02 (1921).
11. Davis, D. M. & Engelder, T. in *Dynamical Geology of Salt and Related Structures* (eds Lerche, I. & O'Brien, J. J.) 301–337 (Academic, 1987).
12. De Bremaecker, J. Cl. Thrust sheet motion and earthquake mechanisms. *Earth Planet. Sci. Lett.* **83,** 159–166 (1987).
13. Brune, J. Particle motions in a physical model of shallow angle thrust faulting. *Proc. Indian Acad. Sci.* **105,** 197–206 (1996).
14. Andrews, D. J. & Ben-Zion, Y. Wrinkle-like slip pulse on a fault between different materials. *J. Geophys. Res.* **102,** 553–571 (1997).
15. Cotton, J. T. & Koyi, H. A. Modelling of thrust fronts above ductile and frictional detachments: Application to structures in the Salt Range and Potwar Plateau, Pakistan. *Geol. Soc. Am. Bull.* **112,** 351–363 (2000).
16. Ford, M. Depositional wedge tops: Interaction between low basal friction external orogenic wedges and flexural foreland basins. *Basin Res.* **16,** 361–375 (2004).
17. Jaumé, S. C. & Lillie, R. J. Mechanics of the Salt Range–Potwar Plateau, Pakistan: A fold-and-thrust belt underlain by evaporites. *Tectonics* **7,** 57–71 (1988).
18. Seeber, L. & Armbruster, J. G. in *Geodynamics of Pakistan: Geological Survey of Pakistan* (eds Farah, A. & DeJong, K. A.) 131–142 (1979).
19. Quittmeyer, R. C. & Jacob, K. H. Historical and modern seismicity of Pakistan, Afghanistan, Northwestern India, and Southeastern Iran. *Bull. Seismol. Soc. Am.* **69,** 773–823 (1979).
20. Abbasi, I. A. & McElroy, R. Thrust kinematics of the Kohat Plateau, Trans-Indus Salt Range, Pakistan. *J. Struct. Geol* **13,** 319–327 (1991).
21. McDougall, J. W. & Hussain, A. Fold and thrust propagation in the western Himalaya based on a balanced cross-section of the Surghar range and Kohat Plateau, Pakistan. *AAPG Bull.* **75,** 463–478 (1991).
22. Engdahl, E. R., van der Hilst, R. & Buland, R. Global teleseismic earthquake relocation with improved travel times and procedures for depth determination. *Bull. Seismol. Soc. Am.* **88,** 722–743 (1998).
23. Engdahl, E. R. & Villaseñor, A. in *International Handbook of Earthquake and Engineering Seismology, Part A* (eds Lee, W. H. K., Kanamori, H., Jennings, P. C. & Kisslinger, C.) Chapter 41, 665–690 (Academic, 2002).
24. Mona, L., Khwaja, A. A & Qureshi, S. N. Structural interpretation on the basis of focal mechanism studies in the area of Kohat Plateau, Bannu Basin and Western Extension of Salt Range. *Pak. J. Hydrocarbon Res.* **15,** 43–51 (2005).
25. Mohadjer, S. *et al*. Partitioning of India–Eurasia convergence in the Pamir Hindu Kush from GPS measurements. *Geophys. Res. Lett.* **37,** L04305 (2010).
26. Sammis, C. G. & Rice, J. R. Repeating earthquakes as low-stress-drop events at a border between locked and creeping fault patches. *Bull. Seismol. Soc. Am.* **91,** 532–537 (2001).
27. Templeton, D. C., Nadeau, R. M. & Burgmann, R. Behavior of repeating earthquake sequences in Central California and the implications for subsurface fault creep. *Bull. Seismol. Soc. Am.* **98,** 52–65 (2008).
28. Johnson Lane, R. & Nadeau, R. M. Asperity model of an earthquake: Static problem. *Bull. Seismol. Soc. Am.* **92,** 672–686 (2002).
29. Hetland, E. A. & Simons, M. Post-seismic and interseismic fault creep II: Transient creep and interseismic stress shadows on megathrusts. *Geophys. J. Int.* **181,** 99–112 (2010).

Acknowledgements

The authors thank S. P. Arun, M. Furuya, P. Molnar, B. Engdhal, G. Ekström, M. Lisa and M. Simon for discussions. Synthetic aperture radar data were provided by the European Space Agency through Category-1 project no 3163. This work was initiated while S.P.S. was a Cooperative Institute for Research in Environmental Sciences Visiting Fellow at the University of Colorado, Boulder, and was completed at the National Geophysical Research Institute, Hyderabad. R.B. was supported by National Science Foundation grant EAR3473959.

Author contributions

S.P.S. undertook the Insar analysis, Z.Y. undertook the seismic analysis, and all three authors drafted the article.

Additional information

The authors declare no competing financial interests. Supplementary information accompanies this paper on www.nature.com/naturegeoscience. Reprints and permissions information is available online at http://www.nature.com/reprints. Correspondence and requests for materials should be addressed to R.B.

nature geoscience

SUPPLEMENTARY INFORMATION

DOI: 10.1038/NGEO1373

Stick-slip advance of the Kohat Plateau in Pakistan

Satyabala S. P. , Zhaohui Yang and Roger Bilham

Contents

1. Supplemental data 1: Rupture parameters and geology

Table S1 Summary of parameters of the 5 May 1992 (122032.85) earthquake and teleseismically recorded aftershocks from various sources.

	Lat ° N	Lon ° E	Depth Km	Strike °N	Dip°	Rake°	Length km	Width km	Slip m	Mw	Notes
Harvard[1]	32.95	71.27	15	237	5	79				6.0 Mw	CMT
USGS[2]	33.377	71.317	16	319	28	164				6.2 Mw	20 May
PDE[3]	33.38	71.32	16							6.3 Mw	20 May
Aftershock1	33.29	71.54								4.6 Mb	31 May
Aftershock2	33.24	71.23								4.9 Mb	5 June
Aftershock3	33.30	71.37								4.4 Mb	9 June
Engdhal et al. 1998	33.30	71.316	22.3±0.71							5.9 Mb	20 May 12:20:35
(ref. 4)	33.311	71.432	26.8±8.5							4.5Mb	11:12:53
Aftershock1	33.214	71.336	19±2.2							5.0Mb	00:22:43
Aftershock2											
Engdhal et al. 2002 [a] (ref. 5)	33.323	71.350	16							6.1 Mw	20 May
MonaLisa et al. (2005) (ref. 6)	33.25	71.30	10	358	64	3				6.0Mw	nodal fit poor
Waveform modeling -this study			8±1	60 (56-64)	87 (84-89)	90 (80-100)				5.9Mw	details below
InSAR [b, c, d] -this study	33.34 note 3	71.26	7.73 (5.6-9.2) note 4	244 (237-249)	1.0 (0.0-4.2)	90	9.9 (4.3-14.5)	8.0 (3.9-11.6)	0.33 (0.19-0.87)	5.9 Mw (5.91-6.02)	details below

[a] "Centennial Catalog"

[b] Values in brackets are parameter ranges of 1σ, but these are not necessarily paired (where 1σ is the standard deviation ~7-mm in the far-field of the interferogram).

[c] The corners of the best-fitting InSAR dislocation are 71.225°E, 33.290°N; 71.320°N, 33.330°E; 71.2879°E, 33.3917°N; 71.1965°N, 33.350°E. The centre of the fault (hypocenter) lies at 7.73 km depth.

[d] 7.8 km is the depth of the lower-left-hand corner of the fault (according to the convention in Okada's expressions) and this is the depth cited in figure S7

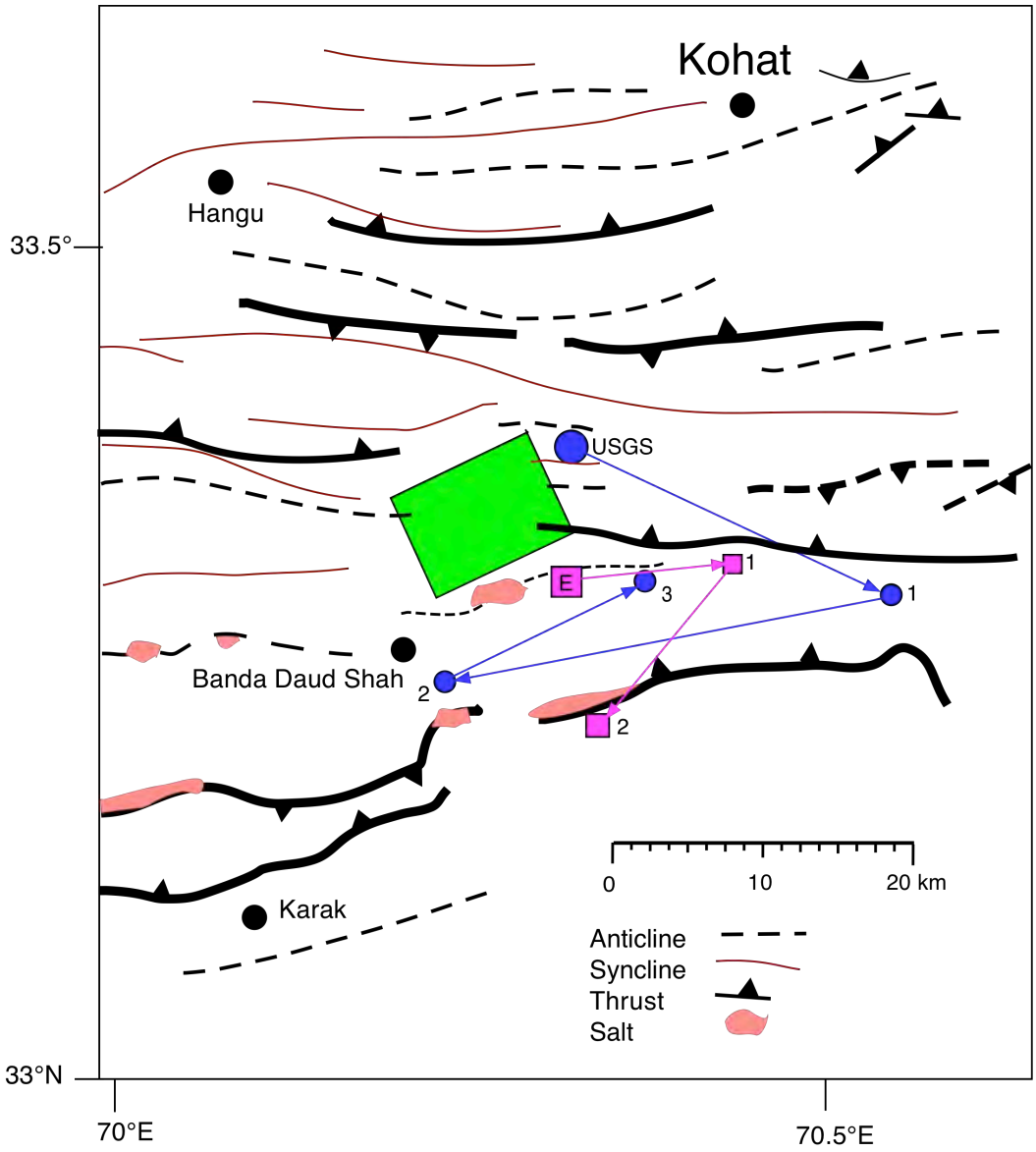

Figure S1 Geological map after Sercombe et al. 1998 (ref. 7) showing location of rupture plane (green oblique square) and teleseismic epicentral locations of mainshock and aftershocks (blue – USGS[2] PDE[3]; violet -Engdhal et al., 1998 (ref. 5)). The aftershocks are numbered sequentially as in Table 1. Teleseismic mislocation biases are of the order of 10 km to the east and southeast. We were unable to satisfactorily undertake waveform analysis of the two aftershocks but we assume, perhaps incorrectly, that they occurred at a similar depth to the mainshock. The Banda Daud Salt is Eocene in age and is not thought to be derived from the basal decollement[8-9].

2. Supplemental Data 2. Seismic waveform modeling

We use waveforms recorded by stations at distances of 30°-90° and 30°-80° for *P* and *S* waves, respectively, to determine the source parameters of the event 920520. At these distances, complications due to major seismic discontinuities bounding the mantle transition zone or from the core-mantle boundary are minimal (Figure S2).

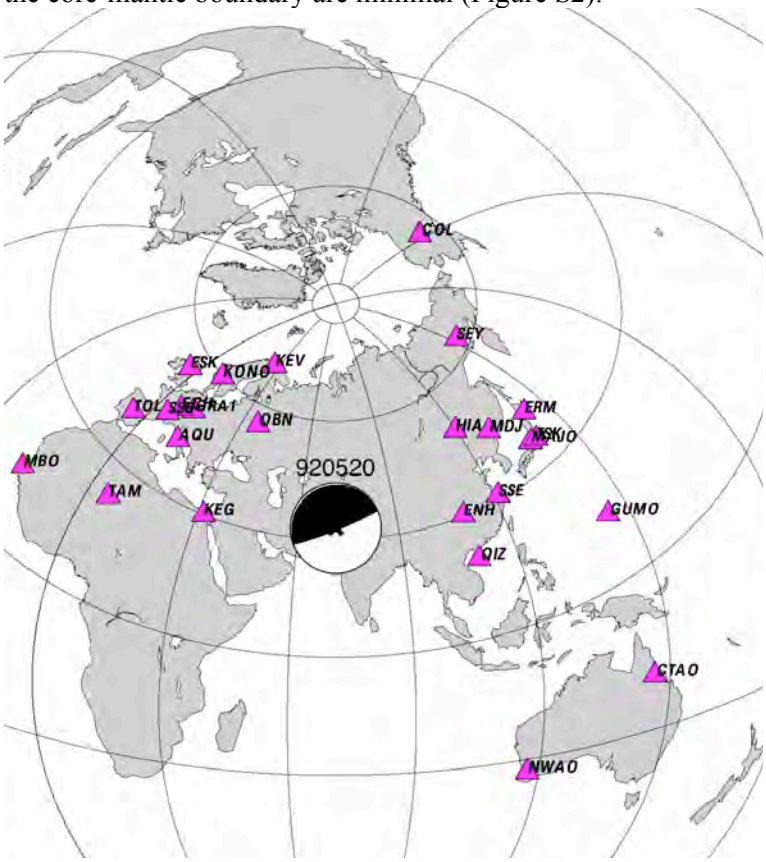

Figure S2 Station Distribution used for re-determination of focal mechanism and depth.

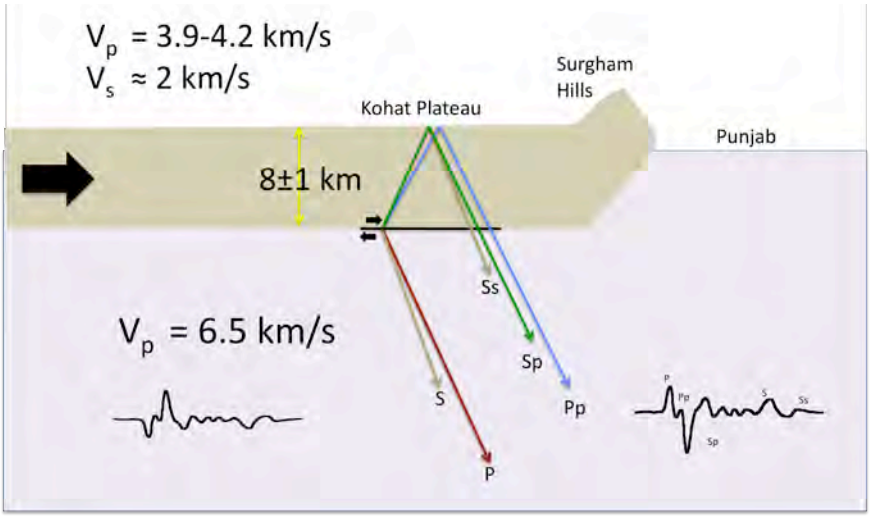

Figure S3 Schematic section through the Kohat plateau showing the geometry of wave paths and phases used in this study and the best fitting depth determined from the adopted velocities, and named phases.

Table S2. Summary of station parameters for the seismograms used for event 920520

Station	Lat. (°)	Lon. (°)	Az. (°)	Dist. (°)	Available Waveforms
COL	64.9	-147.7933	16	77.8	P,S
SEY	62.933	152.373	33	57.3	P,S
HIA	49.2667	119.7417	51	39.3	P
MDJ	44.6164	129.5919	58	46.0	P
ERM	42.015	143.1572	58	56.2	P,S
MAJO	36.5457	138.2041	66	54.1	P,S
TSK	36.2108	140.1097	66	55.7	P,S
SSE	31.0956	121.1867	79	42.0	P,S
ENH	30.2718	109.4868	84	32.5	P,S
GUMO	13.5893	144.8684	87	69.1	P,S
QIZ	19.0294	109.8433	102	37.1	P,S
CTAO	-20.0882	146.2545	115	88.9	P
NWAO	-32.9277	117.239	142	78.5	P,S
BNG	4.435	18.547	252	56.7	S
KEG	29.9275	31.8292	276	33.7	P,S
TAM	22.791	5.527	278	58.2	P,S
MBO	14.391	-16.955	281	80.9	P,S
AQU	42.354	13.405	299	46.0	P,S
TOL	39.8814	-4.0485	300	59.4	P,S
SSB	45.279	4.542	304	51.8	P,S
ECH	48.216	7.158	308	49.6	P,S
GRA1	49.6919	11.2217	310	46.8	P,S
ESK	55.3167	-3.205	318	55.1	P,S
OBN	55.1146	36.5674	323	32.8	P,S
KONO	59.6491	9.5982	323	48.0	P,S
KEV	69.7553	27.0067	340	44.2	P,S

We modeled the amplitude and relative timing between depth phases, *pP*, *sP*, and *sS* and direct arrivals, *P* and *S* in the observed seismograms[10-11] (Figure S3). The differential timing between depth *pP* and *P* phases is twice the ratio between the focal depth, *h*, and the average *P* wave speed between the earthquake and the source. Usually, there is a trade-off between the seismic wave speed and the focal depth. In our case, three depth phases, *pP*, *sP* and *sS,* can be identified on multiple stations simultaneously, constraining an average *Vp/Vs* ratio of 2.0±0.02 for an extremely wide range of *Vp* 1 km/s to 6.5 km/s. Such a large *Vp/Vs* ratio suggests a sedimentary lithology. The relationship between the Vp/Vs ratio and lithology is well established both from laboratory experiments and case studies (e.g. ref. 12). According to the laboratory results, a *Vp/Vs* ratio of 2.0±0.02 corresponds to shale, which has an average *Vp* of 4.0 km/s (ref. 13). Geological studies of the plateau suggest that shale is common in the plateau sediments. Giving this velocity, the focal depth is determined to be 8 km with ±1 km uncertainty given a 10% variation of velocity.

For each phase related to P waves, its amplitude changes systematically according to the orientation of two mutually perpendicular nodal planes, the true fault plane and auxiliary plane. In particular, the ground motion switches polarity across each nodal plane[14]. As stations straddle on both sides of the high-angle nodal plane, the change of *P*-wave's polarity from positive at station ERM to negative at station TSK, provides a strong constraint on the strike and dip of the high-

angle nodal plane. We use both polarity and 10% normalized variance change as the criteria to estimate the uncertainties for the parameters of focal mechanism. The resulted focal mechanism is: strike 60±4, dip 87+2/-3, and rake ±10.

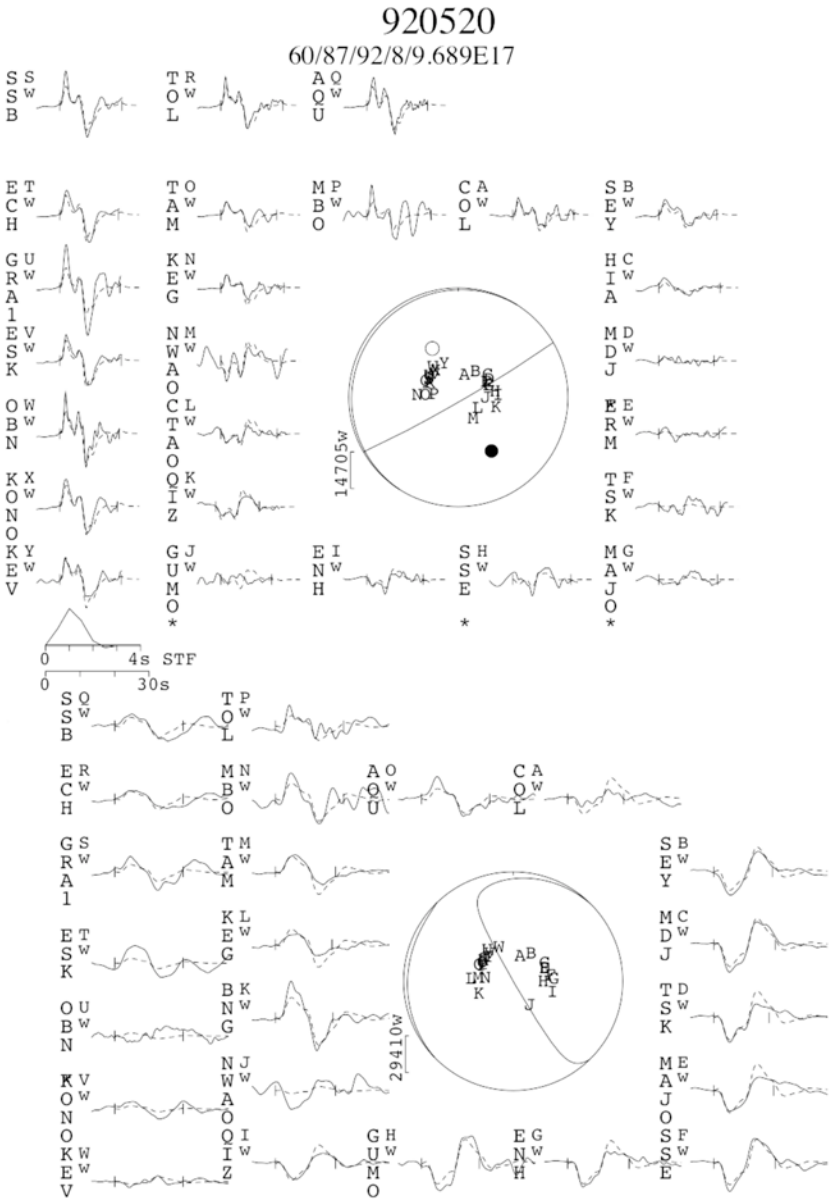

Figure S4 Upper panel *P*-wave and *pP*-wave observations (solid) and synthetic fits (dashed). Center synthetic pulse shape adopted for the fits. Lower panel *S*-wave and *sS* reflected phase observations (solid line) and fits (dashed).

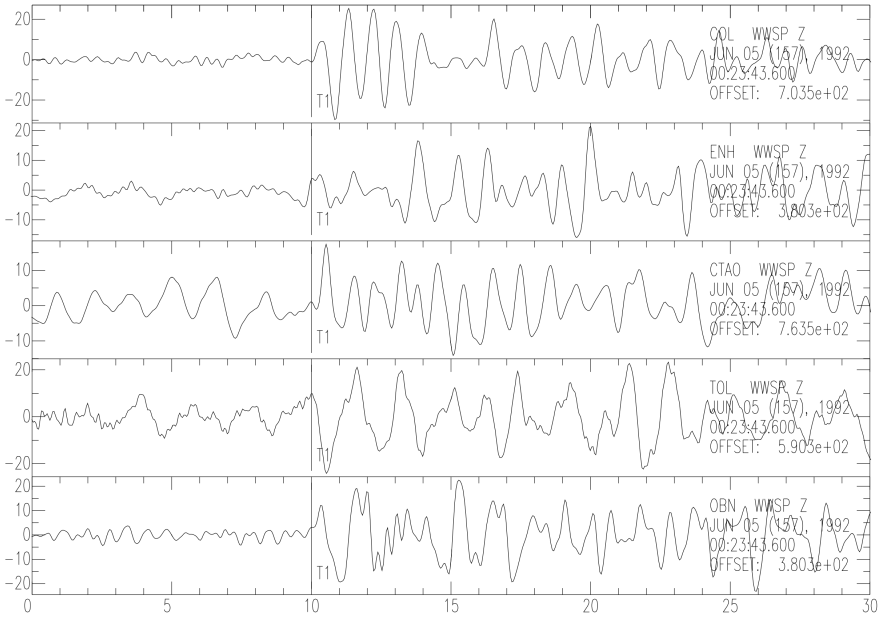

Figure S5 Waveforms from select stations for the 1992 earthquake.

Supplemental Data 3: InSAR processing- Coseismic rupture

We analyzed InSAR data from before and after the Mw6.0 earthquake of 20th May1992 in both the tracks 5 & 277 (Table S3, Figure 6). The Kohat earthquake of 20 May 1992 was captured in both the tracks but in each track we had only one image that was acquired before the earthquake, and no orthogonal tracks are available. Our InSAR analysis includes the use of precision ERS orbit data from the Delft Institute for Earth Oriented Space Research[15] [www.deos.tudelft.nl/], removal of topographic phase simulated using Shuttle Radar Topography Mission (SRTM-3) topographic data (posting at 3 arc sec; http://srtm.usgs.gov), phase-unwrapping followed by baseline refinement to remove residual phase trends across the interferograms and elimination of elevation dependent phase delays. All InSAR processing was done using the software from Gamma Remote Sensing AG (http://www.gamma-rs.ch).

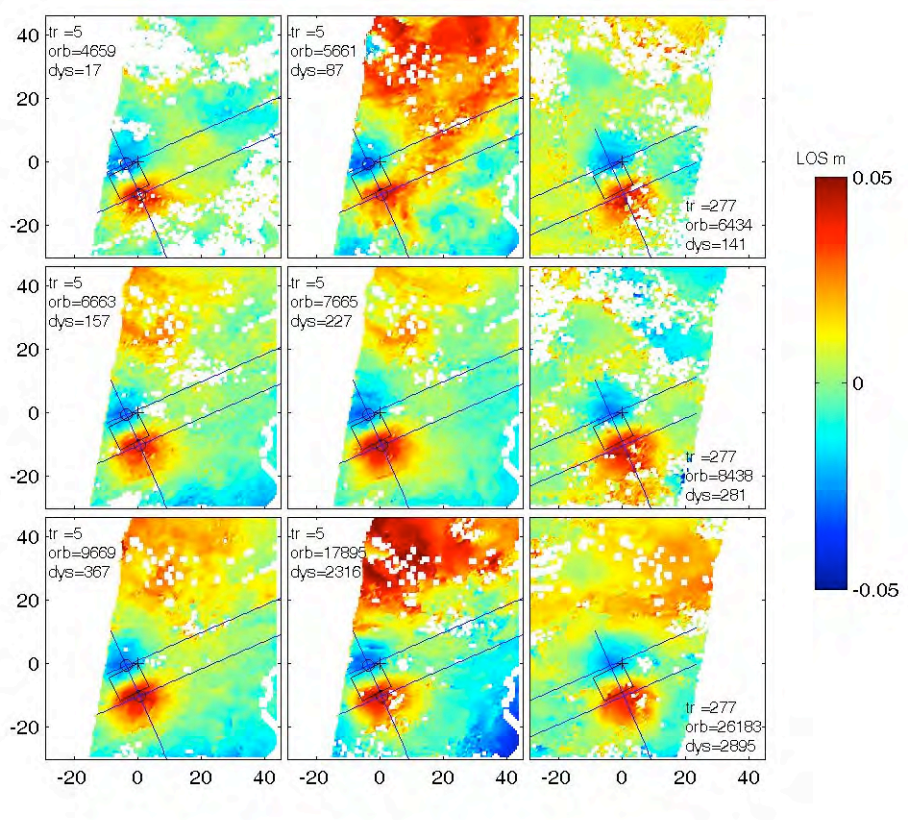

Figure S6 (a): Coseismic interferograms from track 5 (left two columns), track 277 right column. Each figure is marked with the orbit number and the number of days after the earthquake of the second image of the pair.

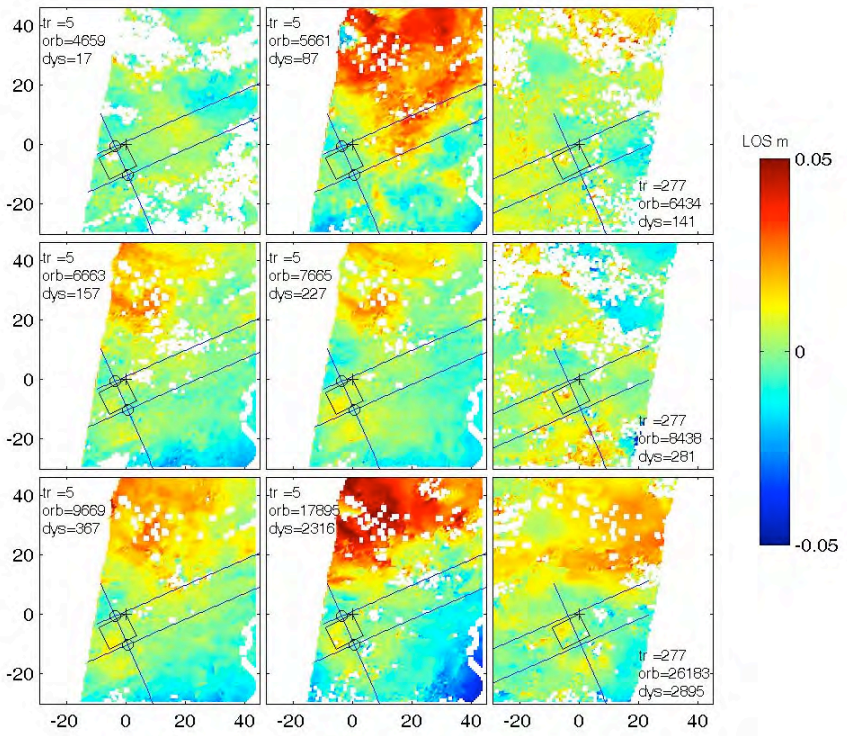

Figure S6 (b) Residual interferograms obtained by subtracting the best-fitting model from each of the coseismic interferograms of figure S6a.

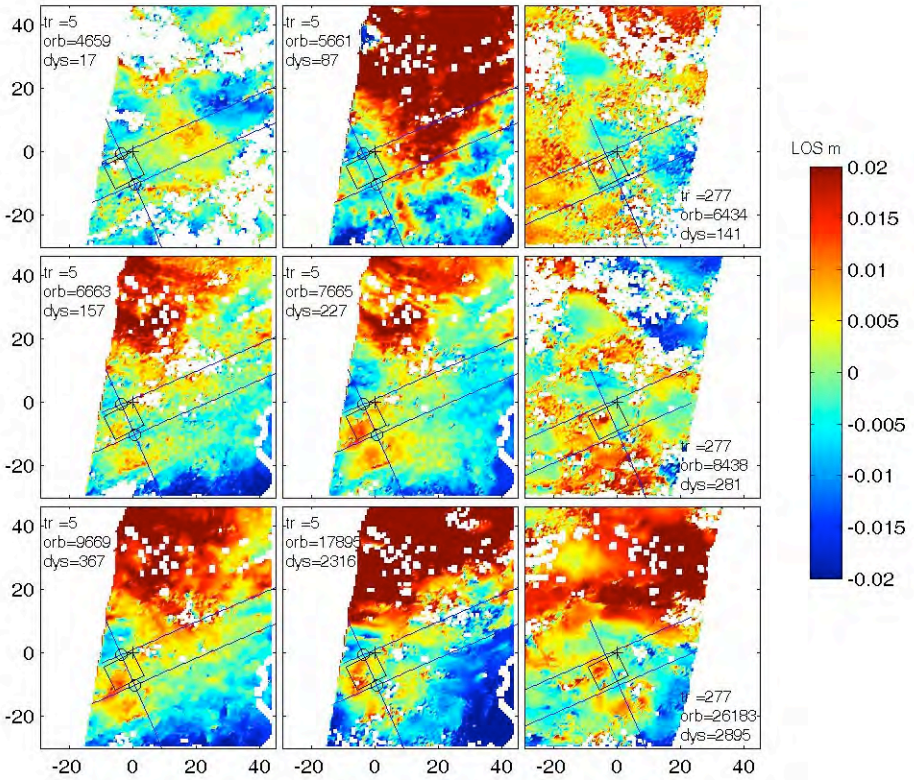

Figure S6 (c): Same as S6(b) but with a different LOS scale to amplify the postseismic creep signal.

Several coseismic interferograms (figure S6) were formed spanning different time intervals ranging from 35-days (17-days after the earthquake) to ~8-years. The 157-day interferogram has the best coherence among these. We modeled the deformation (Table S1) as a planar dislocation in an elastic half-space[16]. The pattern of deformation in different interferograms, while being characteristic of thrust motion on a shallow north-dipping fault, shows differences in spatial extent. Although we fitted models to each interferogram independently, significant residual fringes remained. After several iterations we found that the best model for 157-day interferogram leaves almost no residual fringes in the 17-day interferogram and is also the best fit for all the others (Figure 6a). Figure S6(b) shows the residual interferograms for different time intervals.

We note that the depth (7.8 km) and dip (1°N) are both well-constrained (Figure S7 and Table S1) to ±2 km and ±2° respectively The uncertainties were obtained by undertaking a grid search with a wide range of parameters and subsequently with a series of fine searches using an n-dimensional convex hull algorithm of Matlab software[17-18] to locate the region in parameter space to perform the search. We iteratively searched for model-misfits of less than 2σ (where σ is the standard deviation ~7-mm in the far-field of the interferogram). The parameter space and trade-offs are depicted in figures S7(a, b). The range of best-fitting models shown in Figure S7(c) (and listed in Table S3) suggest that 33 cm of slip occurred on a shallow thrust fault that we presume to be the décollement beneath the Kohat plateau.

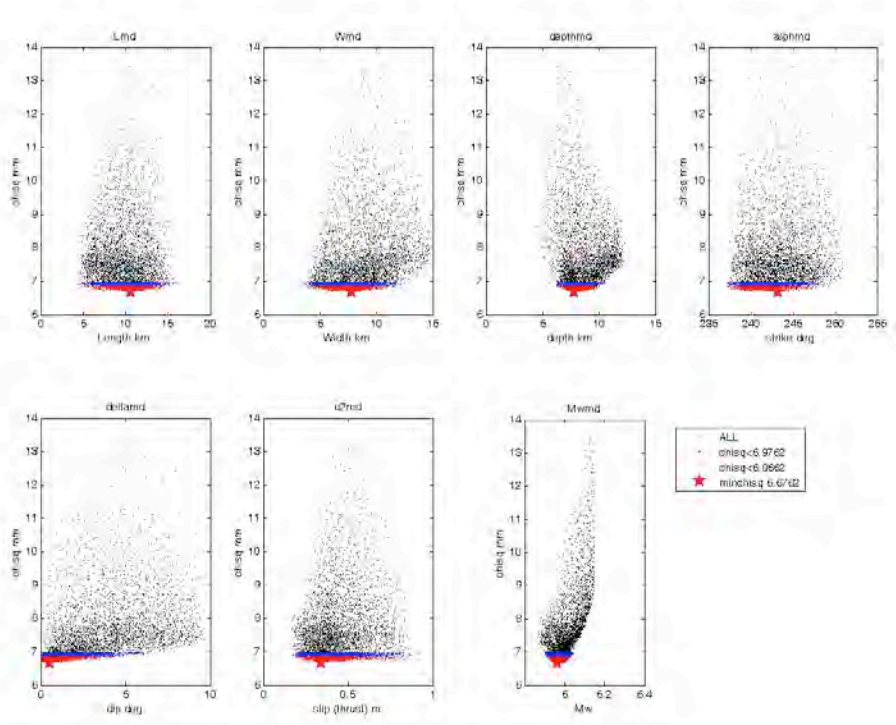

Figure S7 (a) Showing the range of model parameters examined (Length, width and depth in km, strike in degrees clockwise from North, dip in degrees and slip in meters). Each black dot represents one model and 'chisq' is the error/standard deviation (1-s) in mm of the residual. In all figure residual error is computed for the 167-day interferogram

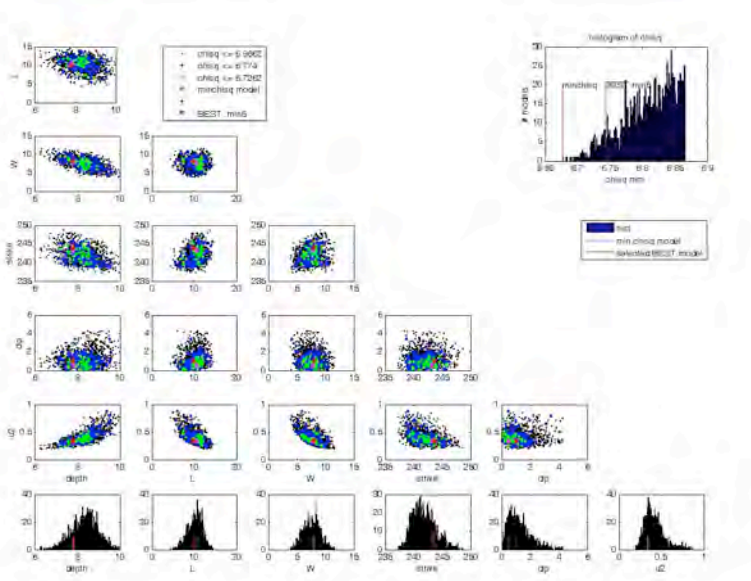

Figure S7 (b): Here the parameter trade-offs are shown. Histograms show the range of models generated but do not necessarily represent uniform sampling of the model space as fine-searches were conducted in the regions of the model space with small error (see text). Different colors are used for models with chi-square error less than a specified value (shown in legend). The red star indicates the preferred model and the pink star indicates the model with minimum chi-square error.

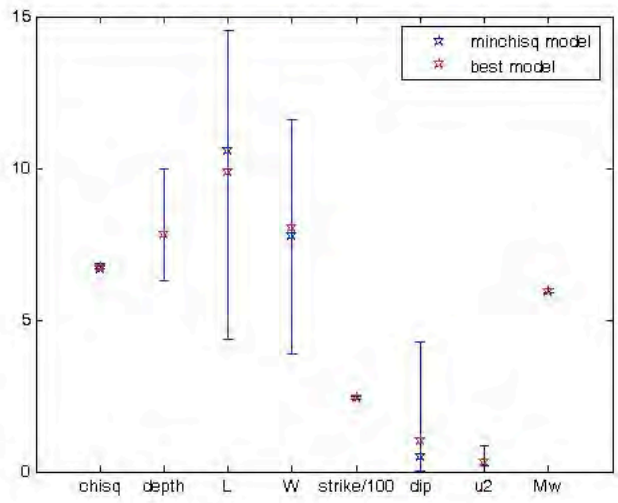

Figure S7 (c) Range (within 1-σ) of fault plane parameters with chisq <6.866-mm (value arbitrarily fixed but representative/lower-than the standard deviation of LOS displacement in the far-field ~7 mm). The red star indicates the preferred model and the blue star indicates the model with minimum chi-square error. Parameters are listed in Table S1.

Supplemental Materials 4 and 5: Post seismic deformation.

In this section we discuss our search for post seismic deformation in several scenes 1992-2000. We summarize our findings as follows: the mean amplitude of afterslip is less than the coseismic rupture by a factor of 3 or more, and its area s confined to the immediate vicinity of the

rupture. An important finding is that afterslip was essentially complete within 6 months of the earthquake.

Supplement 4. Post seismic deformation-unstacked interferograms

While the earliest (17-day) interferogram, can be characterized by slip on a planar rupture, the area of surface deformation evident in successive interferograms increases with time. This suggested to us initially that a post seismic increase in rupture area had occurred, or that additional post-seismic slip had occurred on the rupture plane. However, these subsequent interferograms could not be modeled by an incremental increase in rupture area with uniform or increased slip, suggesting that the post seismic deformation captured by the InSAR scenes does not represent continued afterslip on the main rupture. The best-fitting solution (in a least-squares sense) listed in Table S1 is a single model with the lowest least-squares-error for all inteferograms, that admits that the post-seismic deformation is not well characterized by a planar dislocation model. We estimate that as much as 10% of the post-seismic deformation remains in the form of unmodeled residual fringes.

Figure S8(b) shows the profiles collocated with topography, and demonstrates that the interferogram of 17-days has a nearly flat residual profile (as does its along-strike profile) whereas in the others, two peaks in nearly the same position are visible in different interferograms from two independent tracks (≈2 mm while max-coseismic uplift is ~7-mm of peak to peak). Although these peaks appear to correlate with peaks in topography, residuals near the peak of topography at 0 km (center) and at the left-most peak do not. The plots show that within 17 days of the earthquake there was no deformation (with the exception of co-seismic slip) but in the subsequent interferograms the residuals show some correlation in different interferograms and in two different tracks.

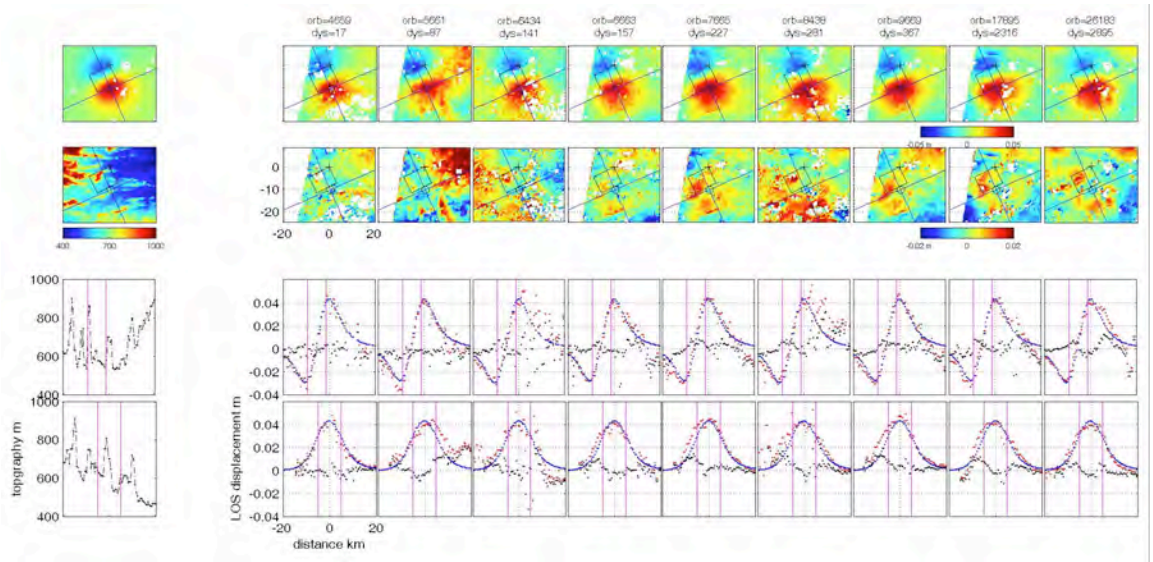

Figure S8 **S8 Top panel:** The model predicted LOS displacement is shown left and the nine adjoining panels are coseismic interferograms showing LOS displacement labeled by orbit number (in tracks 5 & 277) and days after the earthquake (increasing from left to right, see Table S3). The black rectangle in each interferogram shows the modelled dislocation in map view. The black lines show the location of perpendicular profiles drawn in panels (c) and (d). Map coordinates are in UTM projection (origin: location of maximum uplift). Areas with low coherence (< 0.3) are masked out. Magenta vertical lines left show the location of the fault along the profiles.

S8 Second panel : The first is the topography and the nine panels to the right are residual interferograms i.e. InSAR (top panel) minus model-predicted LOS displacement. Magenta vertical lines left show the location of the fault along the profiles.
S8 Third panel : Profiles across the strike of fault. First plot shows topography and the nine adjoing panels are displacement. Raw InSAR profiles = red, synthetic model = blue (shown in S8 (a):left panel), and the residual between the raw and synthetic data indicated by black dots.
S8 Bottom Panel: Profiles of topography and interferometric observations and residuals parallel to strike, through the minimum indicated by the NE/SW line in panel 1.

As the residual fringe amplitudes are of the same order of magnitude as atmospheric contamination in the interferograms, it is tempting to ignore the unmodeled fringes. However, the significant alignment of the residual peaks in two different tracks prompted us to look beyond the widely known processes of postseismic deformations such as continued slip on the mainshock rupture (dismissed above), visco- or poro- elasticity. Following the earthquake, the residual deformation lobes all show a signal which if projected in the direction of slip of the fault rupture of the earthquake, suggest post seismic slip (<2 cm LOS residual i.e. ≈11cm horizontal displacement) on the décollement near the leading and trailing edges of the main rupture. According to our data the main rupture surface remained effectively locked following the mainshock.

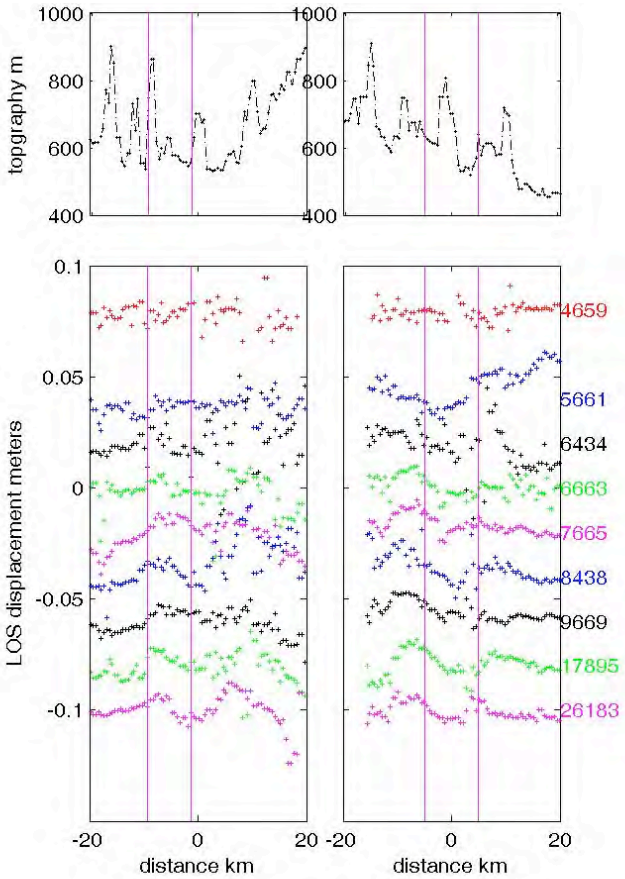

Figure S8(b) Profiles of topography and residual displacement collocated with topography across-strike (a, b) and along-strike of fault(c, d). Scale for (b, d) is shown on left and orbit numbers corresponding to the respective interferograms (listed in Table S3) are shown on the right for each residual plot.

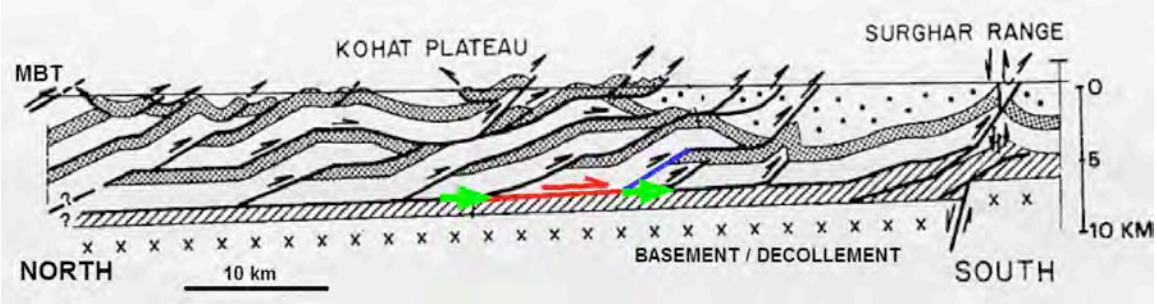

Figure S9: A North-south cross section passing through the Kohat earthquake showing the decollement and (south-dipping) faults branching upwards (section from ref. 19). The spacing between the branching faults is of the order of magnitude of the width of the rupture (thick red line and arrow); blue line highlights splay fault near southern edge of the Kohat earthquake. The InSAR data suggest that accelerated creep was induced on the décollement surrounding the rupture (green arrows).

Supplement 5: Postseismic creep surrounding décollement rupture

On faults that exhibit heterogeneous aseismic creep and stick-slip behaviour, accelerated slip on contiguous segments of the creeping fault frequently follows seismic rupture. Slip is manifest rapidly at first, at rates that decay logarithmically with time[20-22], and the amplitude of this slip may ultimately approach coseismic slip amplitudes[23-24]. InSAR methods have been used widely to monitor these post-seismic slip processes on vertical strike-slip faults[25-31], but have hitherto not been used to quantify afterslip in map view on a shallow horizontal décollement.

We infer, in the body of our article, that slow aseismic slip of the décollement was responsible for pre-seismic loading of the 1992 rupture. Seismic slip at the edges the 1992 Kohat earthquake would have stressed the surrounding décollement, which would have increased the rate of aseismic slip in an annulus surrounding the rupture zone (Figure 3 and Figure S8). In this section we attempt to quantify the areal extent and amplitude of décollement slip following the earthquake.

A cursory inspection of individual postseismic interferograms reveals no clear spatial or temporal pattern indicative of afterslip. This indicates that the amplitude of afterslip is close to the noise level of individual interferograms. Specifically, the combined effects of slip amplitude and its areal extent after the 1992 earthquake resulted in a surface signature that is a fraction of coseismic rupture. To enhance the post seismic signal relative to atmospheric noise in the data we utilized stacking and time-series analysis procedures as described by refs. 32-34.

Twenty one SAR images in track 5 are available of which ten were acquired during 1992-1993, nine during 1998-1999 but only two in the five-year intervening period - in 1996 tandem acquisition (Tables S4 and S5). In track 277 thirteen images are available of which only five span 1992-1993. Because only one image was acquired before the earthquake in each of the tracks, thirty-six postseismic interferograms are available in track 5, but only six are available in track-277. We proceded with an analysis of track 5 because of its promise of a potential factor of six ($\sqrt{n}$) reduction in noise.

We initially used all available images in the analysis despite anomalous atmospheric artifacts evident in some (e.g. in images 3, 4, 5 in Table S4). In a subsequent section we test the influence of noisy scenes on the resulting stacks by incrementally excluding some from the analysis and the effect of baseline decorrelation.

Pre-Processing of post-seismic interferograms

We processed all 210 possible interferograms and selected those with baselines ≤850 m for the interval 1992-1993 and baselines ≤ 300m for the postseismic interferograms spanning 1992-1999. We first eliminated residual orbital errors by fitting a linear ramp to the unwrapped interferograms, a correction that applies globally to the entire interferogram. We next suppressed linear slopes near the rupture area (approximately four fault dimensions corresponding to the area shown in Figure S11) caused by local long-wavelength tropospheric gradients. In order eliminate these tilts/trends we fitted a local linear ramp by masking out areas outside this region. We recognize that this procedure will also eliminate regional gradients caused by linear décollement creep that may also have occurred, but we seek a local perturbation of the creep signal with wavelengths of the order of one fault dimension. These locally detrended interferograms were subsequently used for further analysis. Because of the five year gap in the time series after 1993, we used only the postseismic interferograms formed from images of 1992-1993 in subsequent analysis. Thus of 36 possible pairs, we used 30 postseismic interferograms selected to have baselines less than <850 m. In the presence of a time-invariant signal a stack of the multiple interferograms reduces incoherent noise relative to the static signal by the square root of the number images stacked. Hence our subset of 30-postseismic interferograms is accompanied by an anticipated enhancement in signal to noise of approximately 5.5.

Stacking

Stacked postseismic interferograms, weighted according to their sampling interval (for only those pixels with correlation >0.3 in all interferograms), yield a pattern of continued slip with peaks largely to the NW and SE of the fault that ruptured (figure S11). The pattern resembles those shown in Figures 3 and S8.

Significantly, no evidence for continued slip of the 1992 rupture is apparent in the post seismic stack. Had this occurred it would have resulted in a negative lobe spatially coincident with the coseismic negative lobe for which we see no evidence. We interpret the observed "positive-only" property of the post-seismic signal as accelerated slip induced on the décollement surrounding the rupture.

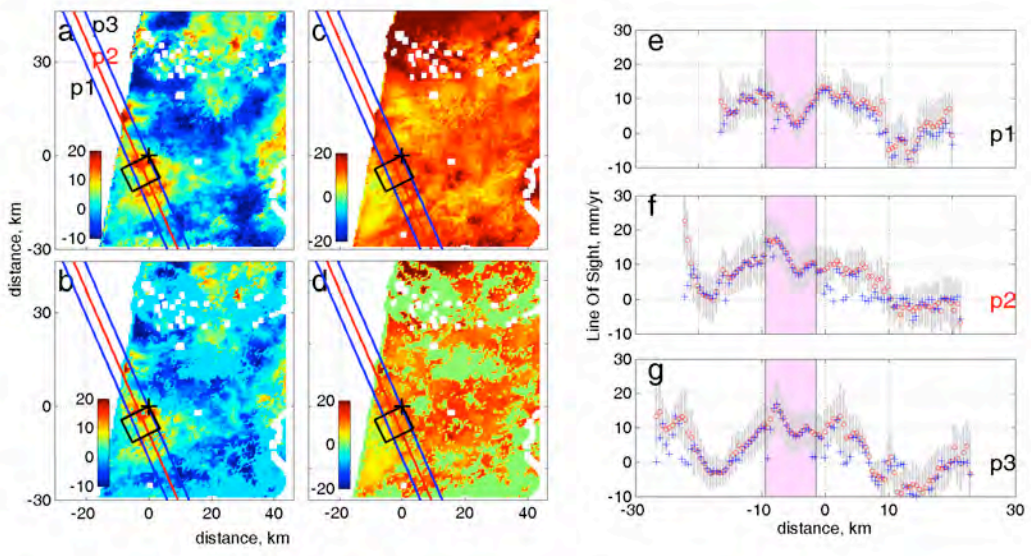

Figure S11: Post seismic stacking (a) compared with post-seismic time series analysis (b). c & d are the corresponding standard deviations associated with a & b respectively. The locations of line of sight profiles p1, p2 and p3 (panels e, f & g) are shown in (a) for time-series analysis

(red circles) and stacking (blue crosses). Error bars correspond to the standard deviation from time-series analysis. The rupture location is shown by a black rectangle on the maps and shaded pink on all profiles. Units for color-scale are rate (a,b) in LOS mm/year and standard deviation (c,d) in mm. The 30 scenes span approximately one year postseismically and hence the rate scale approximates displacement (mm) after one year. Stacking reveals postseismic deformation rate with two peaks with maximum rate 12±4 mm/yr SE of the rupture & 17±4 mm/yr NW of the rupture, and time series analysis reveals a peak of 17±7 mm/yr in each of these quadrants. The standard deviation of phase of the set of interferograms is ~9 mm.

Time Series Analysis

Induced contiguous slip (typically, but somewhat confusingly, described as afterslip in a strike-slip fault setting[23] is however, expected to grow, rapidly at first and then with decreasing speed. i.e. it does not obey the static signal approximation effectively enhanced by simple stacking. We used a time series analysis approach to search for this anticipated decay in rate. The method uses a singular value decomposition analysis for each pixel of the set of interferograms to obtain the best-fitting time-series of deformation that will approximate the set of interferograms used used[34]. A brief outline of this procedure is given below.

Our time series analysis takes the observed range changes (**d**) for each location in a set of interferograms and uses them to infer the underlying displacements (**m**) at that location. Specifically, let d_1, d_2,…d_n be the observed range changes which are taken as elements of the vector **d**. Let r_1, r_2,…be the underlying rates of displacement during the epochs corresponding to consecutive images in the data and Δt_1, Δt_2,…be the corresponding time interval. Thus, for an interferogram formed from images i & j, the total displacement according to this model will be $r_i\Delta t_i + r_{i+1}\Delta t_{i+1} + \ldots + r_j\Delta t_j$. As a result, in our 1992-1993 dataset consisting of 30 interferograms constructed using 9 images (including the reference), we have 30 equations for the 30 observed range changes involving 8 unknowns (which are the incremental displacements that have occurred during the 8 time intervals between epochs of the 9 images). The resulting matrix equation has the form:

$$\mathbf{d} = G\mathbf{r},$$

where G is a design matrix that specifies the relationship between d and r, and the displacements are given by $m_i = r_i\Delta t_i$. Because the number of interferograms is typically much larger than the number of displacements, these equations are overconstrained and can always be used to obtain an estimate of the underlying rates (r) in the least-squares sense. If the rank of the design matrix is equal to the number of displacements, then the available interferograms will fully constrain the displacements, resulting in a unique solution that minimizes the least-squared error. This was the case in our data. This equation was solved using singular value decomposition (SVD) using the function ‘mb’ from the Gamma Remote Sensing software. It may be noted that the solution obtained from SVD is always a least-squares solution – it is either unique (if the matrix is full rank), or is one of many least-squares solutions (if the matrix is not full rank). In our data, where the design matrix has full rank, the least-squares solution and the solution from SVD are identical.

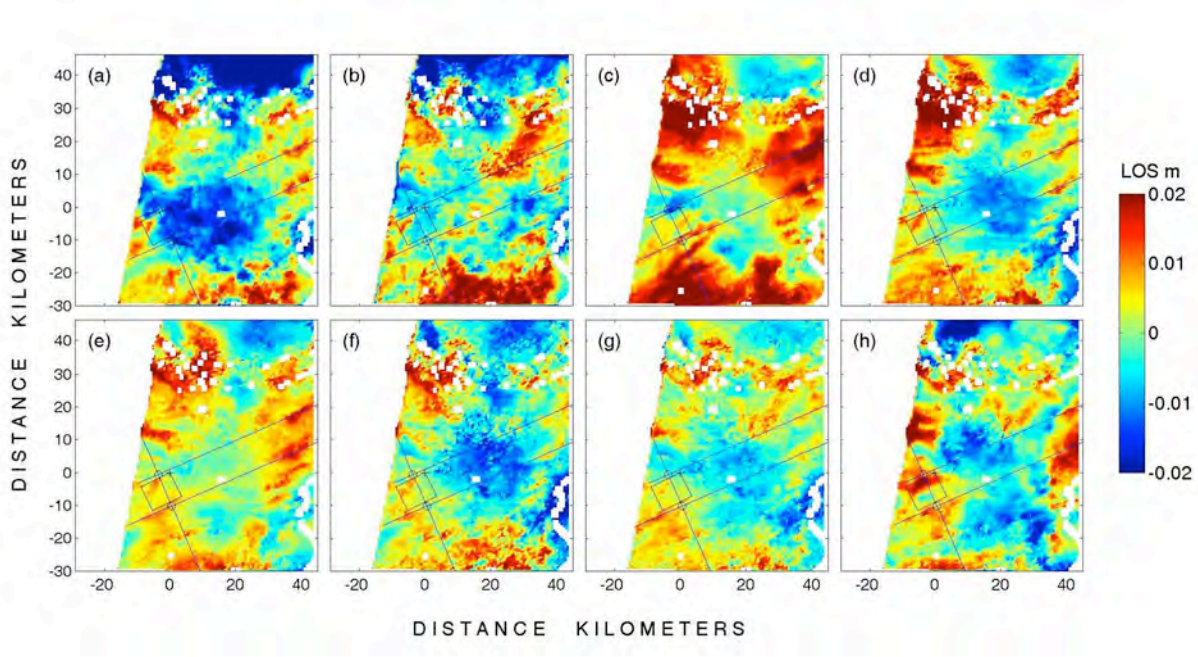

Figure S12a: Sequential growth of afterslip. Time series of range change obtained by inversion of the 30 interferograms. The dates of the time series are: (a-h) are: 19920606_19920711, 19920606_19920815, 19920606_19920919, 19920606_19921024, 19920606_19921128, 19920606_19930102, 19920606_19930522, 19920606_19930626.

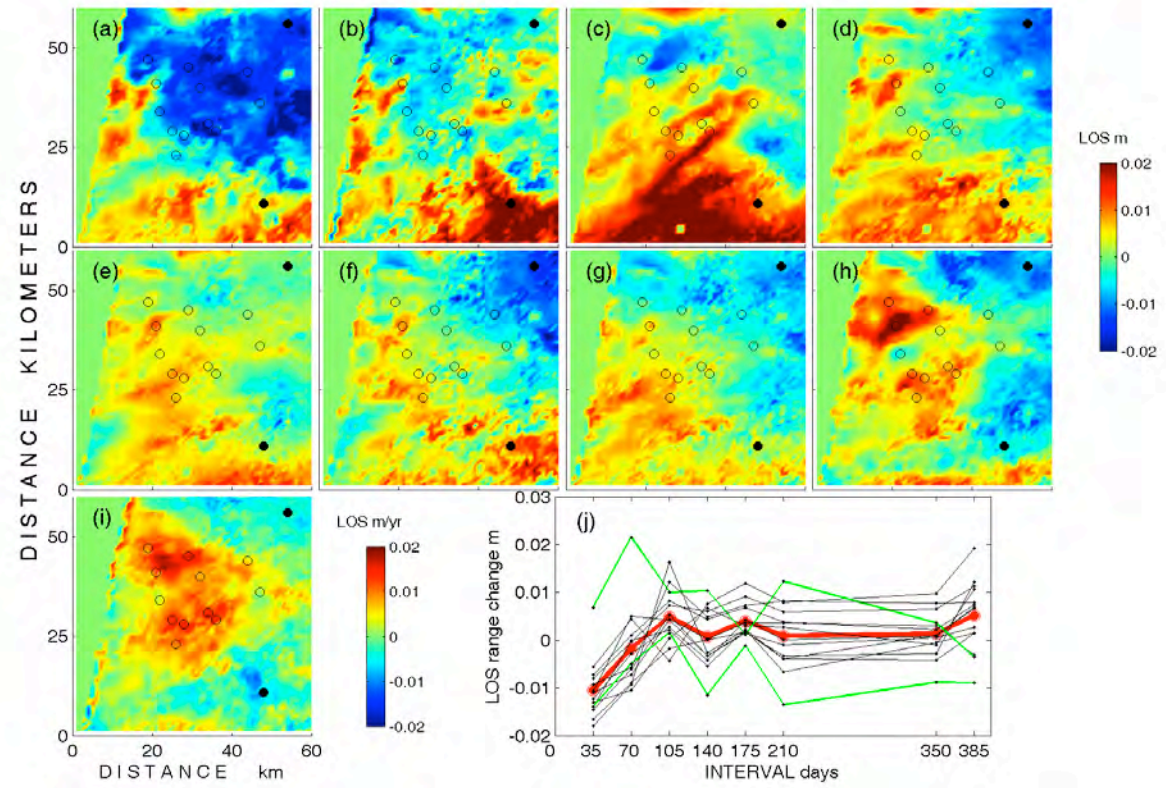

Figure S12b: Time series of deformation for selected pixels. (a-h) same as figure S12a but zoomed into the region of interest, (i) estimated average rate of range change in the ≈ 1 year

following the earthquake (days 35 to 385). Zero on the time axis is 17 days after the earthquake. (j) Plot of range change for selected points, marked by open black circles in (a-j) within the deformation region (black lines); it may be seen that these plots have a similar trend. The average of the range change with time (a-h) of the selected points within the deformation region is shown as a thick dashed red line. It is clear that the afterslip process is non-linear exhibiting rapidly decaying slip after 105 days (equivalent to 122 days following the earthquake as the zero of the time scale above corresponds to the first image dated 19920606 used in the analysis which is 17 days after the earthquake), (Please see last column of table S3). The green lines in (j) are plots of two points (marked by filled black circles in a-j) that lie outside the deformation region; these clearly do not follow this trend.

For the time series analysis we used the same subset of thirty 1992-1993 interferograms used for stacking. The resulting time-series of range change images (Figure S12a), as shown for selected pixels in Figure S12b, do indeed reveal a decaying rate of afterslip as expected from postseismic decay. This decay is clearly visible in panel (j) of Figure S12b which indicates a mean slip rate of ~0.2 mm/day (15 mm in 70 days) in the 122 days after the earthquake. If this occurred linearly, it implies that locally ≈3.6 mm of afterslip may have occurred before the first post-seismic scene (dated 19920606) was acquired 17 days after the earthquake. However, if it occurred as logarithmically-decaying afterslip similar to processes observed elsewhere[21] it would have been substantially more, possibly locally exceeding several cm. We note that afterslip is not evident in the residuals from the coseismic interferogram (Figure S8b). We attribute this to the probable inclusion of early afterslip in our coseismic model discussed below. Our synthetic coseismic dislocation (uniform slip) is unable to precisely model the realistic slip distribution at the edge of the rupture. Specifically we cannot distinguish between tapered (elliptical) mainshock slip, and the increased taper width anticipated from afterslip. The noise in our interferograms precludes further constraints on the temporal pattern of afterslip.

An upper limit to the afterslip "missing" in the afterslip scenes of Fig S11 and S12 is available from the coseismic interferograms, which include these 17 days of early afterslip. We calculated from these scenes a maximum afterslip of <20 mm, which when combined with the afterslip recorded in Figure 12b(i), is consistent with the afterslip we estimate to be "missing" given our stated uncertainties.

Our synthetic coseismic models are consequently almost certainly biased by the inclusion of some afterslip. We speculate that afterslip, given its propensity to "catch-up" with coseismic slip but to not exceed it, would have had the effect of increasing the inferred slip area in the mainshock, but not the slip amplitude. Thus our best-fitting co-seismic rupture probably overestimates the rupture area. Judging by the area involved in subsequent afterslip and its apparent decay with distance, we estimate that our synthetic coseismic rupture area may overestimate the actual rupture area by approximately 10%, with a corresponding small (< 0.05 Mw unit) increase in estimated Mw.

The similarity between the best-fitting least-squares estimate of the rate of deformation from the time series and stacking postseismic creep pattern (Figure S11) is to be expected because the deformation rate obtained represents an average of the deformation during the one year following the earthquake.

Effect of atmospheric contamination on time-series analysis

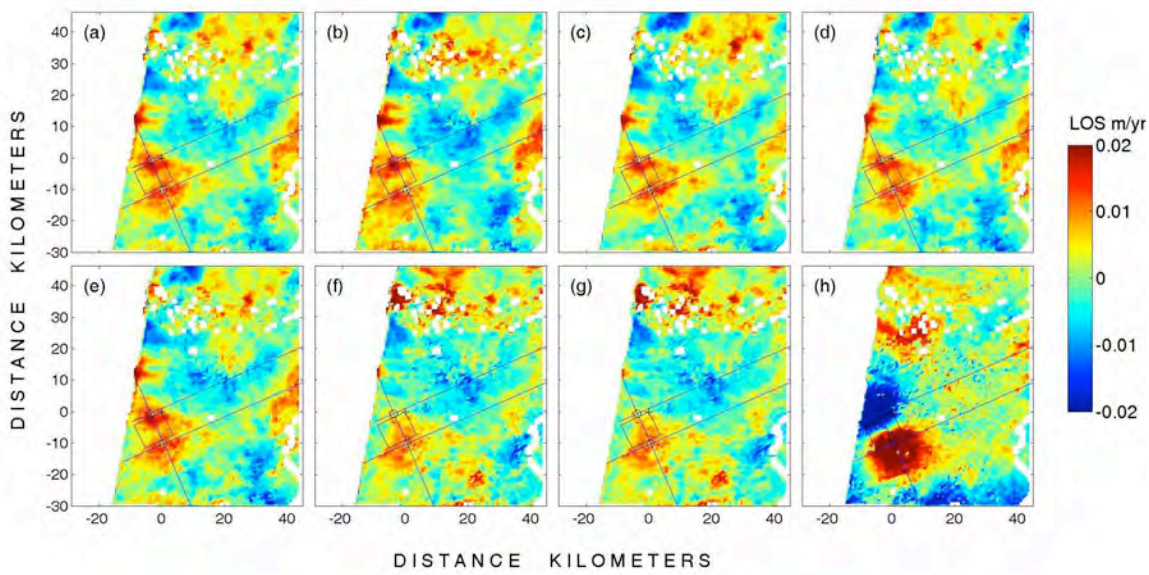

Figure S13: Rate of range-change obtained by time-series inversion excluding selected interferograms. (a) using all 30 postseismic interferograms; (b), (c), (d), (e) and (f) excludes images # 3, 4, 5, 6, 10 respectively, (g) uses all 39 interferograms including coseismic, (h) a coseismic interferogram included for reference. The absence of major differences suggests that the inferred tectonic signature is not unduly influenced by tropospheric noise in any single image.

In order to investigate the effect of significant atmospheric contamination present in all interferograms, we repeated the inversion selectively masking out interferograms formed from individual scenes. Interferograms corresponding to images # 3, 4, 5 were found to have the strongest atmospheric signatures (also seen in the first three images of figure S12). The estimated rate images, after removing these interferograms, are shown in Figure S13.

Contribution from image 10 to the interpretations of postseismic deformation:

Finally, we note that the last interferogram (corresponding to image # 10) appears similar to the result of rate obtained above from stacking as well as from time-series analysis. This shows that the last image of the time-series may be dominating the rate but it is not clear whether this is an atmospheric signature or cumulative deformation. In order to investigate this, we examined all the interferograms formed from this image (Figure S14). If there were a significant atmospheric signature due to this image, it will show up inverted in the last four. However no such indication is manifest and we rule out the possibility that the obtained rate in figure S11 is completely atmospheric signal although contamination to some extent cannot be ruled out.

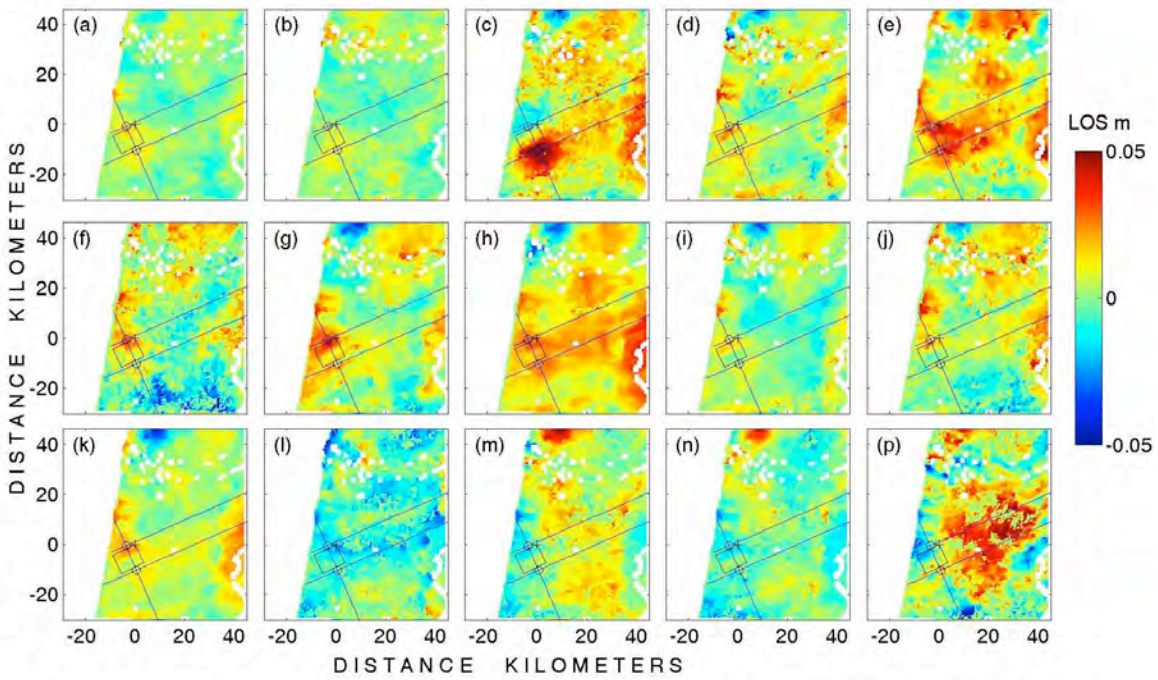

Figure S14: Display of interferograms formed from image #10 corresponding to 19930626. (a) and (b) are rate of range-change obtained by time-series inversion of all postseismic interferograms and by masking image 10 respectively (same as a & e of previous figure). These are shown for reference. (c-p) are interferograms (image pair interval days) = (19920502_19930626 420), (19920606_19930626 385), (19920711_19930626 350), (19920815_19930626 315), (19920919_19930626 280), (19921024_19930626 245), (19921128_19930626 210), (19930102_19930626 175), (19930522_19930626 35), (19930626_19980922 1914), (19930626_19990315 2088), (19930626_19990316 2089), (19930626_19990525 2159). Note that c is a coseismic interferogram, d-j are postseismic with the image #10 as second in the pair and (l) to (p) are interferograms with image #10 as the first in the pair, so that we expect atmospheric signatures to be reversed in the latter. Units for colorscale is in m/yr for a & b.

Effect of baseline decorrelation:

The set of interferograms used in this study (total of 39, including 9 coseismic and 30 postseismic interferograms) depicted as a network in time and perpendicular baseline domain (Figure S15) helps visualize the temporal connectivity between interferograms and their baseline lengths. In this section we will analyze the effect of large baseline lengths in the set of interferograms used in this study.

As mentioned in the section on InSAR processing (supplement 3), although precision orbit data was used to eliminate topographic phase in interferograms, small inaccuracies in satellite orbits this baseline introduce roughly linear residual phase trends across the interferograms. These trends were eliminated by a baseline refinement procedure involving a nonlinear least squares method using as input the unwrapped interferometric phase and the topographic data from the DEM. Apart from the resulting differential interferogram free of

orbital and topographic fringes, this procedure yields root-mean-square (RMS) height error, which is an estimate of the deviation of the interferogram-derived topographic map from the DEM and which is useful for analyzing (discriminating between) error contributions due to baseline decorrelation or other errors in differential interferograms[35]. The sensitivity of interferometric phase to topography is measured by the altitude of ambiguity $\mathbf{h_a}$ which is the amount of height change that leads to a 2π change of interferometric phase for a given baseline, given by:

$$\mathbf{h_a} = \lambda\rho \sin\theta / \{2\mathbf{B_{perp}}\}$$

where λ is the wavelength of the radar signal, ρ is the range or distance from the radar aperture to the target, θ is the look angle and $\mathbf{B_{perp}}$ is the perpendicular baseline length[36].

The RMS error expressed as a fraction of a fringe (RMS/$\mathbf{h_a}$) is an estimate (~λ*RMS/**2**ha) of differential contributions to phase for the smaller baselines and for longer baselines increasingly includes effects of baseline decorrelation and errors in the DEM. Considerations of theoretical ERS-1 interferometer performance yields a critical baseline length of 1115m and interferometric phase errors due to system signal to noise ratio and baseline decorrelation may be estimated following Zebker et al. 1994 (ref. 37) for different baseline lengths. These estimates represent a lower bound on decorrelation noise[37]. Other sources that contribute (and predominate for smaller baselines) to phase errors in interferograms are temporal decorrelation, height errors induced by uncertainties in orbit determination and DEM, and differential contributions such as atmospheric contamination and ground deformation. As our interferograms are dominated by atmospheric contamination, we applied stacking only to those pixels that showed a correlation >0.3 in *all* the interferograms, hence suppressing the contribution of those pixels affected by baseline decorrelation in our interferograms.

Figure S16 shows a plot of the RMS errors from precise baseline estimation method applied to all the interferograms used in this study, showing that baseline decorrelation is evident most notably for six interferograms with baselines >550m. This leads to a first order conclusion that baseline decorrelation does not dominate the error budget in our data for baselines <550 m, which is further supported by subsequent analyses that follow. The RMS error expressed as (~λ*RMS/**2**$\mathbf{h_a}$) is an estimate of the uncertainty of phase due to the sum of all noise contributions for each interferogram, e.g. for the 500-600m baseline range ($\mathbf{h_a}$=15-19m) and the plot shows (RMS/$\mathbf{h_a}$) scattered around ~0.3 fringe for the region of postseismic deformation, which translates to ~8.5 mm error (λ=56 mm for ERS SAR). This compares with the standard deviation (9 mm) of the interferograms obtained from stacking (Figure S11).

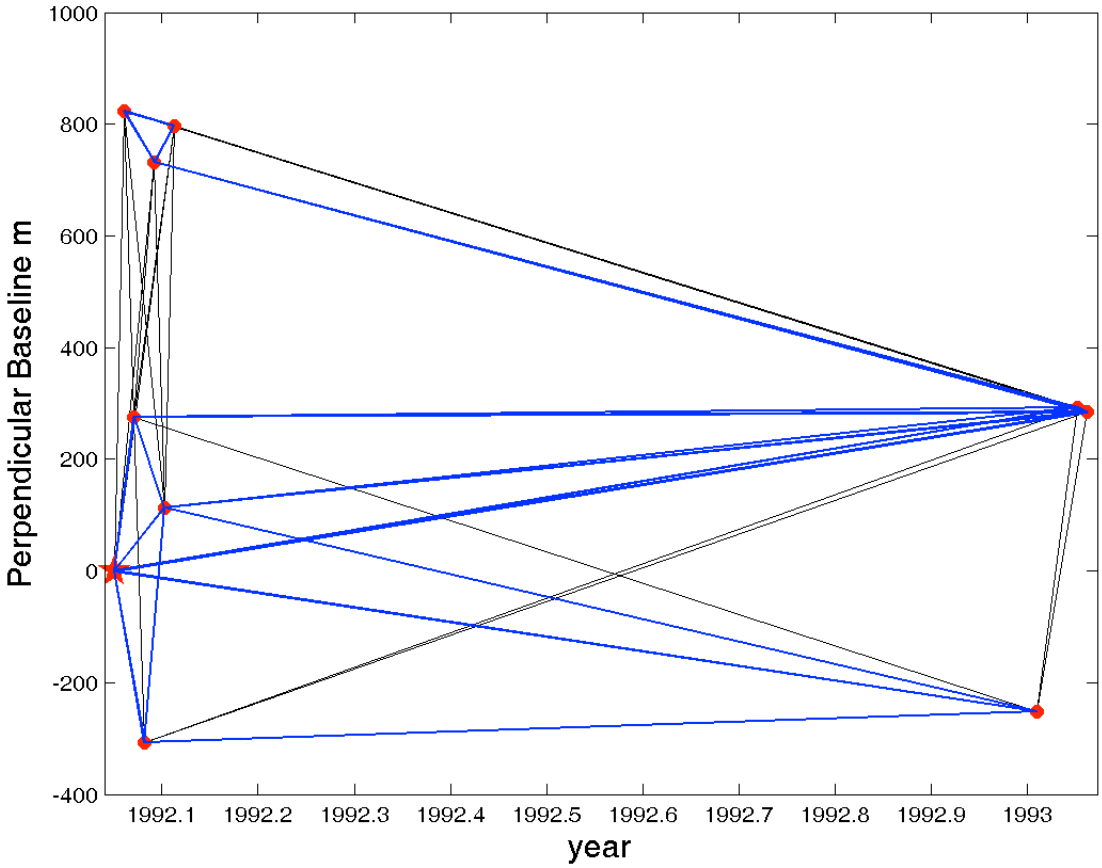

Figure S15. Network of all interferograms spanning 1992-1993 with baselines<850m. The blue lines show baselines ≤420 m, black with baselines>420. For baselines ≥420, the network is connected. The red star indicates the only pre-earthquake image (dated 19920502); the x-axis is the year and y-axis the perpendicular BL in m referenced this image.

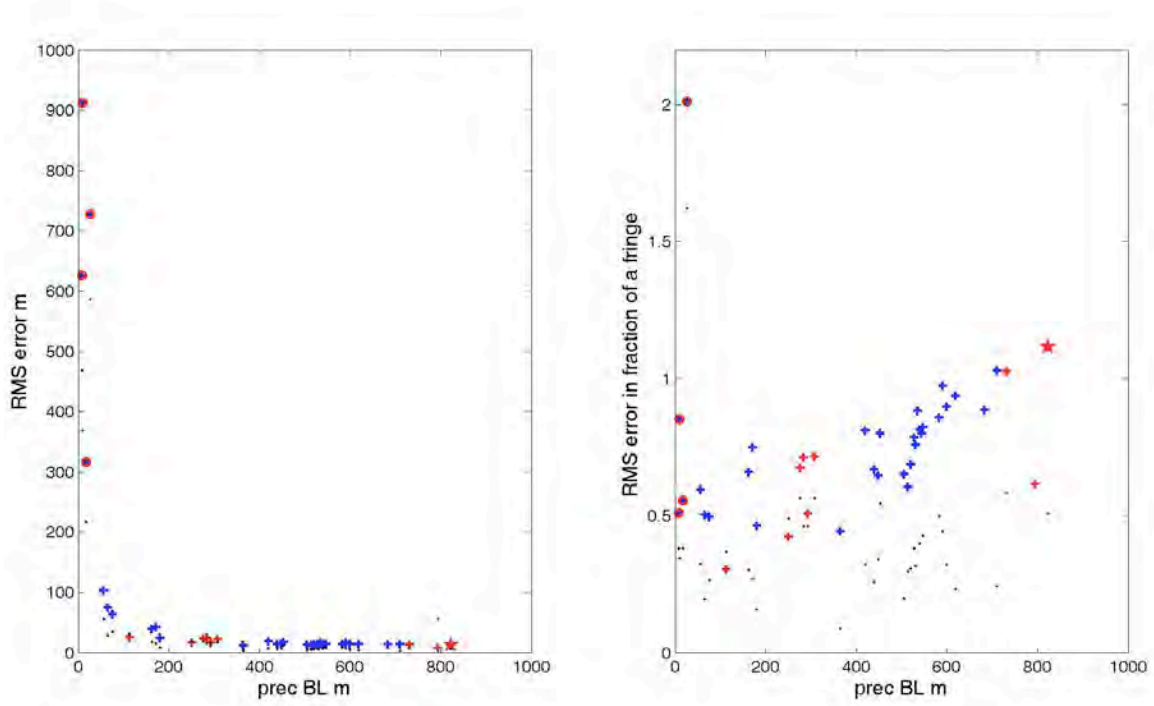

Figure S16: Plots of RMS error in m vs. precise baseline BL (left) and RMS-error expressed as a fraction of a fringe (right), see text for details. The latter is expected to have a constant positive slope if the RMS-errors are purely due to baseline decorrelation; the large scatter for BLs<550m-600m shows that baseline decorrelation is relatively small (unlike the RMS-errors for larger baselines that show a trend) and, for this range of baselines, the errors are mainly due to differential effects (here temporal decorrelation and/or atmospheric contamination). Further, the RMS-errors (black dots) within the region showing the postseismic signal; these errors are smaller as the topography is much gentler here in the rest of the interferogram. Symbols: **blue '+'** for postseismic interferograms, **red '+'** for coseismic interferograms and **black dots** for estimates of RMS in the deformation region. **Star** is the first coseismic interferogram, **Filled red circles**: interferograms with BLs<10m for which RMS errors are very large and we do not interpret them as the inversion is not very stable for such small baselines.

In order to assess the effect of baseline decorrelation noise on the time-series analysis (in the previous section a set of 30 interferograms with large baselines up to 850 m), we repeated the analysis with different baseline cutoffs ranging from 400m-600m but now including the 9 coseismic interferograms to enlarge the data set. The estimated deformation rate maps (Figure S18a) and their standard deviations (Figure S18b) are consistent with a similar pattern suggesting that baseline decorrelation effects do not dominate the time-series inversion results, thereby supporting our conclusion of the presence of postseismic signal.

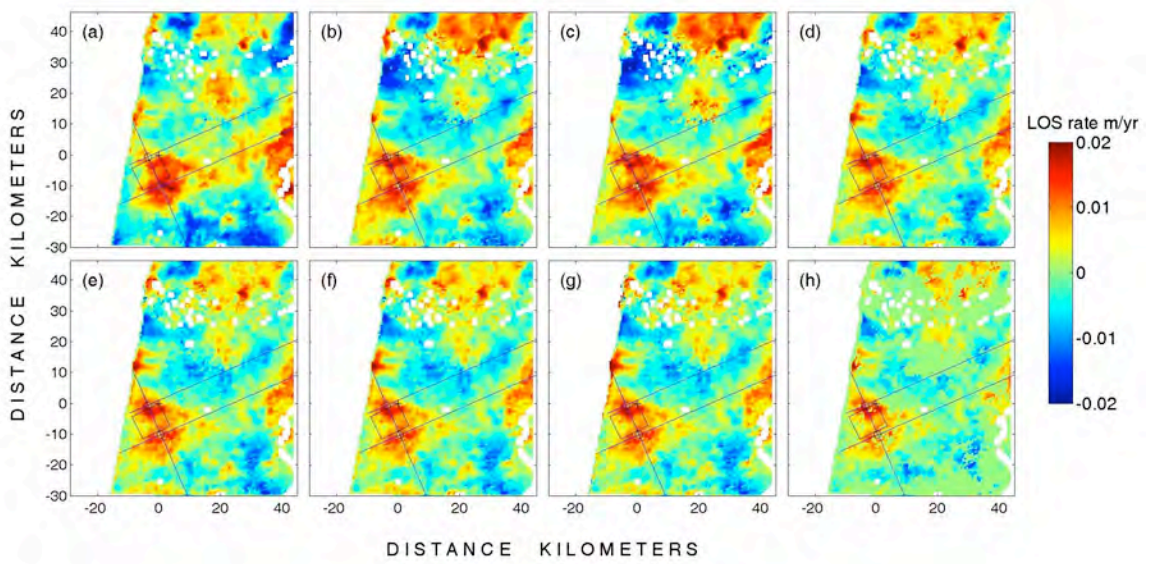

Figure S18a: Effect of different BL cut-offs on the time-series inversion result of postseismic deformation rate using different sets of interferograms selected from of 1992-1993 data of all the 39 interferograms including 9 coseismic interferograms: (a) 17 interferograms selected with BLs<=400m, (b) 20 with BLs<=450m, (c) 21 with BLs<=500m, (d) 30 with BLs<=550m, (e) 33 with BLs<=600m, (f) 39 with BLs<850m. Compare these with the earlier results (g, h) are obtained from the 30 postseismic interferograms with BLs<850 using time-series inversion and stacking respectively. It may be seen that the results are not very much different and, moreover, the amplitude of the results in (g) & (h) presented in the earlier sections is less than with smaller BLs (a-f) implying that the results (g, h) with larger baselines are a lower bound of all different combinations from this data set.

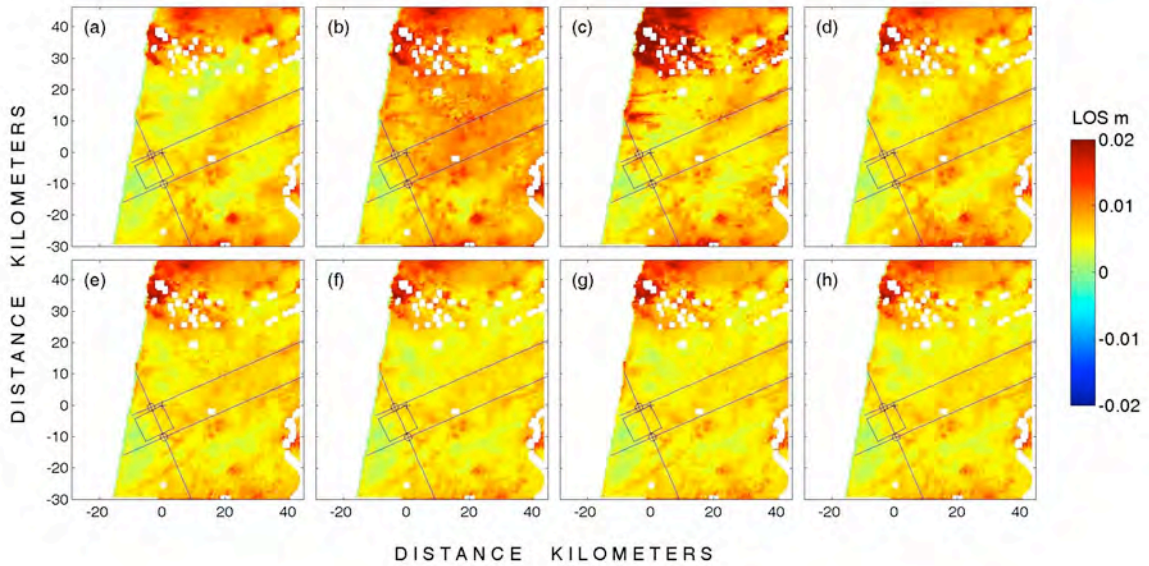

Figure S18b: Standard deviation of rate estimated from the time-series inversion/stacking results in S18a.

Summary of Interpretations of Post-Seismic Interferograms

1. From the coseismic rupture modeling presented in the main body of our article (Figure 3 and Figure S8) we noted a peak postseismic signal of approximately 20 mm.

2. Stacking of post-seismic interferograms in the year following the earthquake quantifies this signal as a peak displacement of 17±8 mm, with an aerial extent of roughly one rupture dimension to the NW and SE of coseismic-rupture.

3. Time series analysis of single pixels reveals 15 mm of afterslip 17-122 days after the earthquake at an average rate of ≈0.2 mm/day and suggests that significant afterslip had occurred before the first postseismic scenes were acquired after the earthquake. Décollement slip was essentially complete in the first half year following the earthquake, typical of afterslip processes observed on creeping faults elsewhere.

4. Post seismic slip on the décollement to the NE and SW of the rupture suggest that afterslip occurred close to the main rupture but not upon it. That is, from the observed pattern it is clear that the 1992 main rupture did not continue to slip. Peak afterslip amplitudes (figure S11) form a rough annulus of positive range-change surrounding the rupture.

5. The presence of rapid post seismic afterslip means that our best-fitting synthetic coseismic model for the 1992 rupture is most probably biased towards a larger rupture area than actually occurred during the earthquake. In principle, models of the afterslip signal could be used to calculate the inside perimeter of the afterslip zone and hence develop an improved coseismic model. In practice, atmospheric noise and the absence of early post-seismic scenes prevents us from conclusively interpreting the temporal evolution of the postseismic creep signal or its spatial extent.

6. Despite shortcomings in the analysis of the details of post-seismic slip, the presence of aseismic afterslip, and an associated distribution of aftershocks, corroborates our conclusion that the 1992 rupture zone was surrounded by a region where pre-seismic creep loaded the main rupture zone towards failure. Continued slip in the region surrounding the main rupture occurred after the earthquake at decreasing rates. We presume that a slow rate of aseismic slip has now resumed.

Table S3:
Coseismic interferograms used for modeling the 20th May1992 Mw6.0 Kohat plateau earthquake.
Here '*Interval days*' is the number of days between of images 1 & 2; '*days after the earthquake'* refers to the acquisition of image 2 with respect to the date of the earthquake listed for coseismic interferograms. The interferograms marked with 'xx'are those coseismic interferograms analyzed but not shown in figure S8.

Interferogram	Image 1			Image 2			Perp BL m	Interval days	Days after the earthquake
	year	month	day	year	month	day			
Track 5									
1. 4158_4659	1992	05	02	1992	06	06	823	35	17
2. 4158_5160 xx	1992	05	02	1992	07	11	275	70	52
3. 4158_5661	1992	05	02	1992	08	15	-306	105	87
4. 4158_6162 xx	1992	05	02	1992	09	19	726	140	122
5. 4158_6663	1992	05	02	1992	10	24	104	175	157
6. 4158_7164 xx	1992	05	02	1992	11	28	791	210	192
7. 4158_7665	1992	05	02	1993	01	02	-251	245	227
8. 4158_9669	1992	05	02	1993	05	22	292	385	367
9. 4158_10170 xx	1992	05	02	1993	06	26	282	420	402
10. 4158_17895	1992	05	02	1998	09	22	254	2334	2316
Track 277									
1. 3929_5432xx	1992	04	16	1992	07	30	-880	105	71
2. 3929_6434	1992	04	16	1992	10	08	-542	175	141
3. 3929_8438	1992	04	16	1993	02	25	-637	315	281
4. 3929_8939xx	1992	04	16	1993	04	01	-659	350	316
5. 3929_26183	1992	04	16	2000	04	23	-195	2929	2895

Table S4: List of Track 5 acquisitions

s.no	orbit	date
1	4158	19920502
2	4659	19920606
3	5160	19920711
4	5661	19920815
5	6162	19920919
6	6663	19921024
7	7164	19921128
8	7665	19930102
9	9669	19930522
10	10170	19930626
11	25043	19960429
12	5370	19960430
13	37568	19980921
14	17895	19980922
15	40073	19990315
16	20400	19990316
17	40574	19990419
18	20901	19990420
19	21402	19990525
20	41576	19990628
21	21903	19990629

Table S5: List of Track 277 acquisitions

s.no	orbit	date
1	3929	19920416
2.	5432	19920730
3	6434	19921008
4	8438	19930225
5	8939	19930401
6	24814	19960413
7	5141	19960414
8	37339	19980905
9	20672	19990404
10	40846	19990508
11	21173	19990509
12	26183	20000423
13	26684	20000528

6. References:

1. Harvard CMT http://www.globalcmt.org/
2. USGS http://earthquake.usgs.gov/
3. PDE http://earthquake.usgs.gov/regional/neic/neic_bulletins.php
4. Engdahl, E.R., and A. Villaseñor, Global Seismicity: 1900–1999, in W.H.K. Lee, H. Kanamori, P.C. Jennings, and C. Kisslinger (editors), *International Handbook of Earthquake and Engineering Seismology*, Part A, Chapter 41, pp. 665–690, Academic Press, (2002).
5. Engdahl, E.R., R. van der Hilst, and R. Buland, Global teleseismic earthquake relocation with improved travel times and procedures for depth determination, *Bull. Seism. Soc. Am*. 88, 722–743, (1998).
6. MonaLisa, Azam. A. Khwaja and Shahid N. Qureshi, Structural Interpretation on the Basis of Focal Mechanism Studies in the Area of Kohat Plateau, Bannu Basin and Western Extension of Salt Range, *Pak. J. Hydrocarbon Res.*, 15, 43-51, (2005).
7. Sercombe, W.J., D.A. Pivnik, W.P. Wilson, M.L. Albertin, R.A. Beck and M.A. Stratton, Wrench Faulting in the northern Pakistan foreland, *AAPG Bull.*, 82, 2003-2030, (1998).
8. Meissner, C. R., Master, J. M., Rashid, M. A. and M. Hussain, Stratigraphy of the Kohat Quadrangle, *Pakistan. USGS Prof. Paper* 716D, (1974).
9. Chen, L., and Khan, S.D., Geomorphometric features and tectonic activities in the Western Himalayan Fold and Thrust Belt: *Computers & Geosciences*, 35 2011-2019, (2009).
10. Langston, C.A., and D.V. Helmberger, A procedure for modeling shallow dislocation sources, *Geophys. J. R. Astron. Soc.*, *42*, 117-130 (1975).
11. Nabelek, J. L., Determination of earthquake source parameters from inversion of body waves, Ph. D thesis, Mass. Inst. of Technol., Cambridge, (1984).
12. Tatham, R.H., and M.D. McCormac, Rock physics measurements, *Multicomponent Seismology in Petroleum Exploration Investigation in Geophysics Series*, 6, Society of Exploration Geophysicists, Tulsa, OK, pp. 43-91, (1991).
13. Christensen, N.I., and D. Stanley, 83 Seismic velocities and densities of rocks, *International Geophysics*, *81*, 1587-1594 (2003).
14. Aki, K., and P.G. Richards, Quantitative Seismology, 2nd ed., 700 pp., Univ. Sci. Books, Sausalito, Calif, (2002).
15. Scharroo, R., and P. N. A. M. Visser, Precise orbit determination and gravity field improvement for the ERS satellites, J. Geophys. Res., 103, 8113–8127, (1998).
16. Okada, Y., Surface deformation to shear and tensile faults in a half-space. , *Bull. Seismol. Soc. Am.*, 75 (4), 1135-1154, (1985)
17. Barber, B., Dobkin, D.P. & Huhdanpaa, H., The Quickhull Algorithm for Convex Hull, *The Geometry Centre Technical Report GCG53*, The Geometry Centre, Univ. of Minesota, Minneapolis, MN 55454, (1993).
18. Sambridge, M., J. Braun and H. McQuenn, Geophysical parametrization and interpolation of irregular data using natural neighbours, Geophys. *J. Int.*, **122,** 837–857, (1995)

19. McDougall, J. W., and A. Hussain, Fold and thrust propagation in the western Himalaya based on a balanced cross section of the Surghar range and Kohat Plateau, Pakistan: *AAPG Bulletin,* 75, 463–478, (1991).
20. Smith, S. & M. Wyss, Displacement on the San Andreas fault subsequent to the 1966 Parkfield earthquake, *Bull. seism. Soc. Amer*., **58** 1955-1973, (1978).
21. Marone, C.J., C.H. Scholz and R. Bilham, On the Mechanics of earthquake afterslip, *J. Geophys. Res*., 96, 8441-8452, (1991).
22. Du, W., L.R. Sykes, B.E. Shaw, and C.H. Scholz, Triggered aseismic fault slip from nearby earthquakes, static or dynamic effect? *J. Geophys. Res.,* 108, 2131, doi:10.1029/2002JB002008, (2003).
23. Bilham, R., Surface slip subsequent to the 24 November 1987 Superstition Hills, California, earthquake monitored by digital creepmeters, *Bull. Seism. Soc. Am*. **79**, 424–450, (1989).
24. Sharp, R. V., K. E. Budding, J. Boatwright, M. J. Ader, M. G. Bonilla, M. M. Clark, T. E. Fumal, K. K. Harms, J. J. Lienkaemper, D. M. Morton, B. J. O'Neill, C. L. Ostergren, D. J. Ponti, M. J. Rymer, J. L. Saxton, and J. D. Sims, Surface faulting along the Superstition Hills fault and nearby faults associated with the earthquakes of 24 November 1987, *Bull. Seism. Soc. Am*. **79**, 252–281, (1989).
25. Massonnet, D., Feigl, K., Rossi, M. and Adragna, F., Radar Interferometric Mapping Of Deformation In The Year After The Landers Earthquake. *Nature,* **369** (6477) :227-230, (1994).
26. Donnellan, A., Parker, J. W. and Peltzer, G., Combined GPS and InSAR models of postseismic deformation from the Northridge earthquake. *Pure And Applied Geophysics,* **159** (10) :2261-2270, (2002).
27. Cakir, Z., de Chabalier, J. B., Armijo, R., Meyer, B., Barka, A. and Peltzer, G., Coseismic and early post-seismic slip associated with the 1999 Izmit earthquake (Turkey), from SAR interferometry and tectonic field observations. *Geophysical Journal International,* **155** (1) :93-110, (2003).
28. Johanson, I.A. & Bürgmann, R., Coseismic and postseismic slip from the 2003 San Simeon earthquake and theireffects on backthrust slip and the 2004 Parkfield earthquake, *J .Geophys. Res*.,115, doi:10.1029/2009JB006599, (2010).
29. Johanson, I. A., E. J. Fielding, F. Rolandone,and R. Bürgmann, Coseismic and postseismic slip of the 2004 Parkfieldearthquake from space-geodetic data, *Bull. Seism. Soc. Am*., 96, 269-282, (2006).
30. Ryder I., B. Parson, T. J Wright and G. J Funning, Post seismic motion following the 1997 Manyo (Tibet) earthquake: Insar observations and modelling, *Geophys. J. Int* **169**, 1009-1027. doi 1`0,1111/j.1365-246X.2006.03312.x, (2007).
31. Biggs, J., Burgmann, R., Freymueller, J. T., Lu, Z., Parsons, B., Ryder, I., Schmalzle, G. and Wright, T., The postseismic response to the 2002 M 7.9 Denali Fault earthquake: constraints from InSAR 2003-2005. *Geophysical Journal International,* **176** (2) :353-367, (2009)..
32. Wright, T., Parsons, B. & Fielding, E., Measurement of interseismic strain accumulation across the North Anatolian Fault by satellite radar interferometry, *Geophys. Res. Lett.,* **28**(6), 2117–2120, (2001).

33. Berardino, P., Fornaro, G., Lanari, R. & Sansosti, E., A new algorithm for surface deformation monitoring based on small baseline differential SAR interferograms, *IEEE Trans. Geosci. Remote Sens.,* **40,** 2375–2383, (2002).
34. Schmidt, D. A., and R. Burgmann, Time-dependent land uplift and subsidence in the Santa Clara valley, California, from a large interferometric synthetic aperture radar data set, *J. Geophys. Res*., 108(B9), 2416, doi:10.1029/2002JB002267, (2003).
35. Satyabala, S. P., Coseismic ground deformation due to an intraplate earthquake using synthetic aperture radar interferometry: The Mw6.1 Killari, India, earthquake of 29 September 1993, *J. Geophys. Res*., 111, B02302, doi:10.1029/2004JB003434, (2006).
36. Rosen, P. A., S.Hensley, I. R.Joughin, F. K.Li, S.N. Madsen, E.Rodriguez, and R. M.Goldstein, Synthetic aperture radar interferometry, *Proc. IEEE*, 88(3), 333– 382, (2000).
37. Zebker, H. A., C. L. Werner, P. Rosen, and S. Hensley, Accuracy of topographic maps derived from ERS-1 radar Interferometry, *IEEE Trans. Geosci Remote Sens*., 3, 2(4), 823-836, (1994).